

ISTANBUL TECHNICAL UNIVERSITY ★ INFORMATICS INSTITUTE

**SPARSITY BASED PANSHARPENING AND A NEW PANSHARPENING
METHOD USING A GUIDING IMAGE**



M.Sc. THESIS

Ronglei JI

Department of Communication Systems

Satellite Communication and Remote Sensing Programme

JUNE 2019

ISTANBUL TECHNICAL UNIVERSITY ★ INFORMATICS INSTITUTE

**SPARSITY BASED PANSHARPENING AND A NEW PANSHARPENING
METHOD USING A GUIDING IMAGE**



M.Sc. THESIS

**Ronglei JI
(705171013)**

Department of Communication Systems

Satellite Communication and Remote Sensing Programme

Thesis Advisor: Assoc. Prof. Dr. Ender Mete Ekşiođlu

JUNE 2019

İSTANBUL TEKNİK ÜNİVERSİTESİ ★ BİLİŞİM ENSTİTÜSÜ

**SEYREKLİK TABANLI PANKESKİNLEŞTİRME VE KILAVUZ GÖRÜNTÜ
KULLANAN YENİ BİR PANKESKİNLEŞTİRME YÖNTEMİ**

YÜKSEK LİSANS TEZİ

Ronglei JI

(705171013)

İletişim Sistemleri Anabilim Dalı

Uydu Haberleşmesi ve Uzaktan Algılama Programı

Tez Danışmanı: Doç. Dr. Ender Mete Ekşioğlu

HAZİRAN 2019

Ronglei Ji, a M.Sc. student of ITU Informatics Institute student ID 705171013, successfully defended the thesis entitled “SPARSITY BASED PANSHARPENING AND A NEW METHOD USING A GUIDING IMAGE”, which he prepared after fulfilling the requirements specified in the associated legislations, before the jury whose signatures are below.

Thesis Advisor : **Assoc. Prof. Dr. Ender Mete EKŞİOĞLU**

Istanbul Technical University

Jury Members : **Assoc. Prof. Dr. Ender Mete EKŞİOĞLU**

Istanbul Technical University

Prof. Dr. Ahmet Hamdi KAYRAN

Istanbul Technical University

Assoc. Prof. Dr. Hacı İLHAN

Yıldız Technical University

Date of Submission : 03 May 2019

Date of Defense : 13 June 2019





To my wife and parents,



FOREWORD

I would like to express my sincere thanks to my thesis supervisor Assoc.Prof. Ender Mete Ekşioğlu for his great supervision and guidance during my graduate studies. His professionalism and faithfulness to academic research give me a good beginning of scientific research.

In addition, I would like to express my deepest thanks and love to my wife for her encourage and accompany in my graduate studies.

May 2019

Ronglei Ji





TABLE OF CONTENTS

	<u>Page</u>
FOREWORD	ix
TABLE OF CONTENTS	xi
LIST OF TABLES	xiii
LIST OF FIGURES	xv
ABBREVIATIONS	xvii
LIST OF SYMBOLS	xix
SUMMARY	xxi
ÖZET	xxiii
1. INTRODUCTION	1
1.1 Purpose of Thesis	3
1.2 Outline of Thesis	4
2. OVERVIEW OF PANSHARPENING METHODS	5
2.1 Component Substitution (CS) category	6
2.2 Multiresolution Analysis (MRA) category	10
2.3 Model based category	12
3. SPARSITY BASED PANSHARPENING	15
3.1 BM3D image model.....	16
3.2 Proposed Guiding-Image-BM3D model	18
3.3 HySure: A model based pansharpening method	20
3.4 Proposed ADMM-GIBM3D pansharpening method	24
4. SIMULATION	27
4.1 Performance measurement	27
4.1.1 Visual evaluation.....	27
4.1.2 Quantitative evaluation with reference	28
4.1.3 Quantitative evaluation without reference	30
4.2 Datasets	32
4.3 Implementation	33
4.4 Results and comparisons	34
4.4.1 Visual comparison.....	34
4.4.2 Quantitative comparisons with reference.....	43
4.4.3 QNR comparisons	45
5. CONCLUSIONS AND FUTURE WORK	49

5.1 Conclusions 49
5.2 Future work 50
REFERENCES 51
CURRICULUM VITAE 57



LIST OF TABLES

	<u>Page</u>
Table 2.1: Different categories of pansharpening methods.....	6
Table 4.1: Visual evaluation for image quality assessment .	27
Table 4.2: Properties of the datasets.....	32
Table 4.3: Quantitative results with reference for DE2 dataset.	43
Table 4.4: Quantitative results with reference for IK dataset.....	44
Table 4.5: Quantitative results with reference for WV2 dataset.	44
Table 4.6: Quantitative results with reference for Moffett dataset.....	44
Table 4.7: Quantitative results with reference for KSC dataset.	45
Table 4.8: Quantitative results without reference for DE2 dataset.	45
Table 4.9: Quantitative results without reference for IK dataset.	46
Table 4.10: Quantitative results without reference for WV2 dataset.	46
Table 4.11: Quantitative results without reference for Moffett dataset.	46
Table 4.12: Quantitative results without reference for KSC dataset.....	47



LIST OF FIGURES

	<u>Page</u>
Figure 1.1: Spatial and spectral differences among PAN, MS and HS image.	1
Figure 1.2: Basic principle of Pansharpening process.....	3
Figure 2.1: Pansharpening flowchart of CS family.	7
Figure 2.2: Pansharpening flowchart of GS method.	8
Figure 2.3: Pansharpening flowchart of GFPCA method.	9
Figure 2.4: Pansharpening flowchart of MRA family.	10
Figure 2.5: Pansharpening flowchart of SFIM method.	11
Figure 2.6: Pansharpening flowchart of Model based family.	12
Figure 3.1: Principle of sparse representation.	15
Figure 3.2: Block-matching of patches into 3D array according to similarity (reference block with thick borders).	17
Figure 3.3: Flowchart of the BM3D denoising algorithm.	18
Figure 3.4: Simplified flowchart of the BM3D denoising algorithm.	18
Figure 3.5: Flowchart of proposed GIBM3D denoising algorithm. (a) GIBM3D-w sub-model, (b) GIBM3D-wth sub-model, (c) GIBM3D-thw sub-model.....	19
Figure 4.1: Flowchart for Wald’s protocol.	28
Figure 4.2 (a): Pansharpened images for DE2 dataset: (a) REF; (b) PCA; (c) GFPCA; (d) GS; (e) GSA; (f) HPF; (g) SFIM; (h) HySure; (i) ADMM-BM3D; (j) ADMM-GIBM3D;	35
Figure 4.2 (b): Pansharpened image residue with REF for DE2 dataset: (a) REF; (b) PCA; (c) GFPCA; (d) GS; (e) GSA; (f) HPF; (g) SFIM; (h) HySure; (i) ADMM-BM3D; (j) ADMM-GIBM3D;	36
Figure 4.3 (a): Pansharpened images for IK dataset : (a) REF; (b) PCA; (c) GFPCA; (d) GS; (e) GSA; (f) HPF; (g) SFIM; (h) HySure; (i) ADMM-BM3D; (j) ADMM-GIBM3D;	36
Figure 4.3 (b): Pansharpened image residue with REF for IK dataset: (a) REF; (b) PCA; (c) GFPCA; (d) GS; (e) GSA; (f) HPF; (g) SFIM; (h) HySure; (i) ADMM-BM3D; (j) ADMM-GIBM3D;	37
Figure 4.4 (a): Pansharpened images for WV2 dataset: (a) REF; (b) PCA; (c) GFPCA; (d) GS; (e) GSA; (f) HPF; (g) SFIM; (h) HySure; (i) ADMM-BM3D; (j) ADMM-GIBM3D;	37
Figure 4.4 (b): Pansharpened image residue with REF for WV2 dataset: (a) REF; (b) PCA; (c) GFPCA; (d) GS; (e) GSA; (f) HPF; (g) SFIM; (h) HySure; (i) ADMM-BM3D; (j) ADMM-GIBM3D;	38
Figure 4.5 (a): Pansharpened images for Moffett dataset: (a) RF; (b) PCA; (c) GFPCA; (d) GS; (e) GSA; (f) HPF; (g) SFIM; (h) HySure; (i) ADMM-BM3D; (j) ADMM-GIBM3D;	38

Figure 4.5 (b): Pansharpened image residue with REF for Moffett dataset: (a) REF; (b) PCA; (c) GFPCA; (d) GS; (e) GSA; (f) HPF; (g) SFIM; (h) HySure; (i) ADMM-BM3D; (j) ADMM-GIBM3D;	39
Figure 4.6 (a): Pansharpened image for KSC dataset: (a) REF; (b) PCA; (c) GFPCA; (d) GS; (e) GSA; (f) HPF; (g) SFIM; (h) HySure; (i) ADMM-BM3D; (j) ADMM-GIBM3D;	39
Figure 4.6 (b): Pansharpened image residue with REF for KSC dataset: (a) REF; (b) PCA; (c) GFPCA; (d) GS; (e) GSA; (f) HPF; (g) SFIM; (h) HySure; (i) ADMM-BM3D; (j) ADMM-GIBM3D;	40
Figure 4.7: Spectrum for DE2 dataset.	40
Figure 4.8: Spectrum for IK dataset.	41
Figure 4.9: Spectrum for WV2 dataset.	41
Figure 4.10: Spectrum for Moffett dataset.	42
Figure 4.11: Spectrum for KSC dataset.	42



ABBREVIATIONS

ADMM	: Alternating Direction Method of Multipliers
BM3D	: Block-Matching 3-D
CC	: Cross Correlation
CNN	: Convolution Neural Network
CS	: Component Substitution
DRN	: Deep Residual Network
ERGAS	: Relative Dimensionless Global Error
GAN	: Generative Adversarial Network
GIBM3D	: Guiding Image Block-Matching 3-D
GLP	: Generalized Laplacian Pyramid
GS	: Gram-Schmidt
GSA	: Gram-Schmidt Adaptive
GFPCA	: Guiding Filter Principal Component Analysis
HPF	: High Pass Filter
HS	: Hyperspectral
IFOV	: Instantaneous Field of View
MRA	: Multi-Resolution Analysis
MS	: Multispectral
MTF	: Modulation Transfer Function
PAN	: Panchromatic
PCA	: Principal Component Analysis
PSNR	: Peak Signal-to-Noise Ratio
QI	: Quality Index
QNR	: Quality with No Reference
REF	: Reference
RMSE	: Root Mean Square Error
SAM	: Spectral Angular Mapper
SFIM	: Smoothing Filter-Based Intensity Modulation
VTV	: Vector Total Variation



LIST OF SYMBOLS

α	: Sparse Coefficients
\mathbf{B}	: Blurring Matrix
\mathbf{D}	: Lagrange Multiplier
\mathbf{E}	: A Basis for an Identified Subspace
\mathbf{M}	: Subsampling Operator
\mathbf{N}	: Band's Number
\mathbf{R}	: Spectral Response Matrix
λ_p	: Regularization Parameter
μ	: Regularization Parameter





SPARSITY BASED PANSHARPENING AND A NEW PANSHARPENING METHOD USING A GUIDING IMAGE

SUMMARY

This thesis aims at enhancing spatial resolution quality of multispectral and hyperspectral remote sensing satellite images by utilizing a registered panchromatic image of the same scene. This technique is called as “Pansharpening” in the literature.

High spectral resolution images with high spatial details have wide applications in precision agriculture, forest protection and monitoring, mineral detection, marine and environmental research. However, a single satellite remote sensing sensor cannot acquire images which have both high required spatial resolution and high required spectral resolution as a result of some technical constraints. Pansharpening is an effective image fusion technique to solve this problem by taking advantage of the prevailing properties of both pan image and multispectral or hyperspectral image to generate high spectral resolution images with high spatial details for the purpose of satisfying various demands of remote sensing satellite images.

This thesis firstly gives an overview of different pansharpening methods and briefly classifies the pansharpening methods into the Component Substitution category, the Multi-Resolution Analysis category and the model based category. Some important methods are analyzed and compared in inter- and intra-categories.

The second aim of this thesis is to propose a novel pansharpening approach using the newly developed Guiding Image BM3D image denoising algorithm. BM3D is an effective denoising algorithm. In the proposed algorithm, an external guiding image is added as the basic estimate to the Wiener filtering step of the BM3D algorithm and this forms the three sub-models of the GIBM3D algorithm. In the thesis, the proposed GIBM3D algorithm is applied in a model based pansharpening method. The GIBM3D is implemented in every iteration of the Alternating Direction Method of Multipliers (ADMM) process in this pansharpening model.

For comparisons of different pansharpening methods, visual evaluation, quantitative evaluation with reference images and without reference images are introduced. Then three multispectral and two hyperspectral image datasets are tested to validate the performance of proposed ADMM-GIBM3D approach and to compare the performance of various pansharpening methods.

Experimental results in this thesis have demonstrated that the proposed ADMM-GIBM3D pansharpening method has competitive performance with the existing model based pansharpening methods. The results also show that the three sub-models of the proposed ADMM-GIBM3D method result in almost equivalent performance.



SEYREKLİK TABANLI PANKESKİNLEŞTİRME VE KILAVUZ GÖRÜNTÜ KULLANAN YENİ BİR PANKESKİNLEŞTİRME YÖNTEMİ

ÖZET

Bu tez çalışmasında multispektral (MS) ve hiperspektral (HS) uzaktan algılama uydu görüntülerinin uzamsal çözünürlük kalitesinin artırılması amaçlanmaktadır. Bu problem ve ilgili çözüm yöntemleri literatürde genel olarak “pankeskinleştirme” (pansharpening) başlığı altında incelenmektedir.

Uydu teknikleri ve uygulamaları hızla geliştikçe, artan miktarda uydu uzaktan algılama görüntüleri genel kullanıma sunulmaktadır. Farklı platformlar ve sensörler uydu görüntülerinin çözünürlük kalitesini belirler. Uzamsal detaylara sahip yüksek spektral çözünürlüklü görüntüler, tarım, orman koruma ve izleme, mineral algılama, deniz ve çevre araştırmalarında önemli ve geniş uygulamalara sahiptir. Bununla birlikte, tek bir uydu uzaktan algılama sensörü, bazı teknik kısıtlamalar nedeniyle hem gereken yüksek uzamsal çözünürlüğe hem de yüksek gereken spektral çözünürlüğe sahip görüntüleri elde edemez: 1) Sensöre girecek radyasyon enerjisinin sınırlaması vardır. 2) Yüksek uzamsal kaliteli MS / HS görüntünün veri hacmi çok büyük ölçüdedir. Bu platformda sınırlı veri depolama kapasitesi ve platformdan yer alıcısına iletim bant genişliğinin yetersizliği sorunlarına neden olabilir. Uzaktan algılama ile elde edilen uydu görüntülerinin çeşitli uygulama taleplerini karşılamak için hem yüksek uzamsal çözünürlüğe, hem de yüksek spektral çözünürlüğe sahip olması istenmektedir. Pankeskinleştirme, yüksek uzamsal detaylara sahip ve yüksek spektral çözünürlükte görüntüler üretmek için, hem pankromatik (PAN) görüntüsünün hem de çoklu- spektral veya hiperspektral görüntünün üstün özelliklerinden yararlanarak bu sorunu çözmek için geliştirilmiş etkili bir görüntü füzyon tekniğidir. Bu kaynaştırma işleminde, pankromatik görüntünün uzamsal içeriği ve MS / HS görüntünün spektral içeriği mümkün olduğu kadar korunmalıdır. Böylece kestirilen son görüntünün mümkün olduğu kadar orijinal (aranan) görüntünün hem uzamsal hem de spektral

detaylarını içermesi sağlanabilir. Pankeskinleştirme bunun dışında görüntü yorumlama, nesne tanıma, sınıflandırma ve değişiklik tespiti gibi önemli diğer bazı uydu görüntü temelli uygulamalar için çok önemli bir ön işleme aşamasını oluşturmaktadır.

Bu tezin ilk kısmında, farklı pankeskinleştirme yöntemleri genel bir şekilde incelenmekte ve farklı yaklaşımlar açıklanmaktadır. Pankeskinleştirme yöntemleri Bileşen Değiştirme (Component Sunstitution-CS), Çoklu Çözünürlük Analizi (Multi Resolution Analysis- MRA) ve model tabanlı algoritmalar alt sınıflarına ayrılmaktadır. CS kategorisi, PAN görüntüsünün yüksek çözünürlüklü uzamsal içeriğinin, MS / HS görüntüsünün düşük çözünürlüklü uzamsal içeriğinin yerini almasıyla gerçekleşir. Çoklu Çözünürlüklü Analiz kategorisi genel olarak, PAN görüntü üzerinden pankeskinleştirilmiş MS / HS görüntülerini elde etmek ve uzamsal yapı detaylarını vermek için uzamsal filtreler kullanır. Model temelli pankeskinleştirme yöntemleri kategorisinde ise genel olarak gözlemlenen MS / HS ve PAN görüntülerine ilişkin matematiksel bir model oluşturulur.

Tez kapsamında, literatürde önerilmiş çok sayıda yaklaşım arasından önemli görülen bazı pankeskinleştirme yöntemlerini detaylı şekilde analiz edip karşılaştırdık. CS kategorisinde yer alan pankeskinleştirme yöntemleri MS görüntüler için görece daha iyi uzamsal kalite sağlar. MRA kategorisinde yer alan pankeskinleştirme yöntemleri ise MS görüntüleri için daha iyi spektral kalite üretir. HS pankeskinleştirme açısından, MRA kategorisi genellikle CS kategorisinden daha iyi performans gösterir. Model tabanlı yöntemler hem MS hem de HS pankeskinleştirme için iyi performans gösterir. Bununla birlikte, model tabanlı yöntemler CS ve MRA kategori yöntemleriyle karşılaştırıldığında çok daha fazla işlem zamanı gerektirmektedir.

Bu tez kapsamında geçmişte önerilmiş model tabanlı ve özyinelemeli yöntemlere dayanarak, yeni bir pankeskinleştirme yaklaşımı önerilmektedir. Literatürde daha önce sunulmuş olan Block Matching 3D (BM3D) etkili bir görüntü gürültü giderme algoritmasıdır. Yeni geliştirilen pankeskinleştirme yöntemi, BM3D içinde bir kılavuz görüntü kullanımını ortaya koymaktadır. Böylece Kılavuz Görüntü BM3D (Guiding Image BM3D-GIBM3D) olarak isimlendirdiğimiz, model tabanlı ve özyinelemeli yeni bir pankeskinleştirme yaklaşımı ortaya konulmaktadır.

BM3D, yinelemeli özyinelemeli pankeskinleştirme yöntemleri için literatürde kullanılmış etkili ve güçlü bir görüntü gürültü giderme algoritmasıdır. BM3D algoritmasının Wiener filtreleme basamağında temel bir görüntü kestirimine ihtiyaç duyulmaktadır. Bu tezde, BM3D algoritmasının pankeskinleştirme uygulamasında kullanımının performansını arttırmak için gürültü giderilmiş görüntü kestirimleri yerine, pankeskinleştirme sonucu elde edilmiş harici kılavuz görüntülerinin kullanımı önerilmektedir. Burada önerilen kılavuz görüntü kullanımı, Wiener filtreleme adımının blok eşleştirme aşamasında gruplama performansını artırmakta ve buna ek olarak 3D spektral katsayıların Wiener filtrelenmesinde başarımı iyileştirmektedir. Kılavuz görüntünün kullanımı, Wiener filtreleme adımında daha iyi gruplama ve daha iyi filtreleme için referans olarak işlev görmektedir.

Yukarıda özetlendiği gibi, önerilen yeni Kılavuz Görüntü BM3D (GIBM3D) algoritması Wiener filtreleme adımının temel kestirim girişini harici bir kılavuz görüntü ile değiştirmektedir. Tez kapsamında GIBM3D algoritması için üç ayrı alt model oluşturulmaktadır. Tezde önerilen bu üç farklı GIBM3D algoritması yapısı, model tabanlı ve özyinelemeli bir pankeskinleştirme çerçevesi içinde kullanılarak pankeskinleştirmeye uygulanmıştır. Bu kapsamda GIBM3D, pankeskinleştirme için “Alternating Direction Method of Multipliers” (ADMM) tabanlı özyinelemeli bir algoritmanın yineleme adımlarının bir alt bileşeni olarak gerçekleştirilmektedir. GIBM3D, her bir ADMM yinelemesinde iyileştirilmiş bir görüntü kestirimi oluşturmak için gürültü giderici bir düzenleme (regularization) adımı olarak kullanılmaktadır. Kullanılan kılavuz görüntünün kalitesine göre, ADMM-GIBM3D algoritması tarafından üretilen pankeskinleştirme sonuçları değişiklik göstermektedir.

Tez kapsamında farklı pankeskinleştirme yöntemlerinin karşılaştırılması için görsel değerlendirme ve referans görüntüleri karşılaştırma içeren nicemsel değerlendirmeler yapılmıştır. Referans görüntü ile nicel değerlendirmede, gözlenen görüntü işaretleri referans olarak kullanılan mevcut bir MS / HS görüntüsünden sentetik olarak üretilmektedir. Gözlemi oluşturan görüntüler pankeskinleştirilmekte, ve üretilen sonuç görüntüleri referans ile karşılaştırılarak değerlendirilme yapılmaktadır.

Önerilen ADMM-GIBM3D yaklaşımının ve literatürde sunulmuş farklı tiplerde rakip pankeskinleştirme yaklaşımlarının performanslarını karşılaştırmak için üç adet

multispektral ve iki hiperspektral görüntü veri seti üzerinde kapsamlı benzetimler gerçekleştirilmiştir.

Bu tezin benzetim sonuçları, önerilen ADMM-GIBM3D pankeskinleştirme yönteminin mevcut model tabanlı pankeskinleştirme yöntemleriyle rekabetçi bir performansa sahip olduğunu göstermiştir. Bunun dışında sonuçlar, önerilen ADMM-GIBM3D yönteminin her üç alt modelinin neredeyse eşdeğer performansa sahip olduğunu göstermektedir.



1. INTRODUCTION

As satellite techniques and applications rapidly advance, an increasing amount of satellite remote sensing images are made available to the public. Some commercial satellites like SPOT, LANSAT and IKONOS provide multispectral (MS) with panchromatic (PAN) images, EO and AVIRIS providing Hyperspectral (HS) images [1].

Different platforms and sensors determine the resolution quality of satellite images (Figure 1.1). Regarding the spatial resolution, it represents the measuring ability of the sensor to resolve the smallest object or the measure of the ground area which is imaged into the Instantaneous Field of View (IFOV) of the remote sensing system. Spectral resolution depicts the number of total bands or the spectral width of single band in digital image. PAN image has only one single wide-width band that is located in visible spectrum and some commercial satellites can provide even below a half-meter spatial resolution PAN image. MS image generally has three to more than ten bands in visible to near-infrared wavelengths. However, HS images usually have hundreds of narrower spectral bands [1].

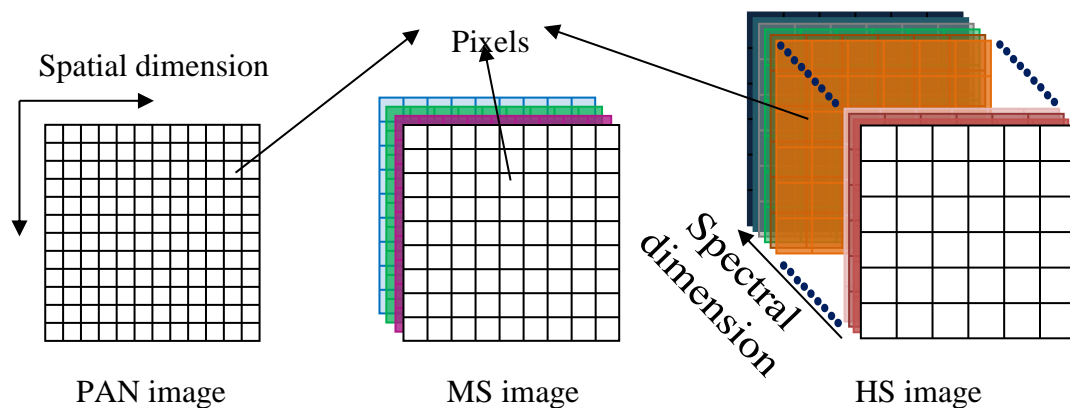


Figure 1.1: Spatial and spectral differences among PAN, MS and HS images.

High spectral resolution images with good spatial quality are widely employed in precision agriculture, forest protection and monitoring, mineral detection, marine and environmental research. In order for better interpretation capabilities and more reliable results, these applications require the satellite remote sensing images to contain rich geometric details and spectral information.

However, images that have high spectral resolution with high spatial details cannot be acquired by a single satellite remote sensing sensor. This is mainly due to the following two restrictions:

(1) There is limitation for incoming radiation energy to be received into the sensor [2]. Generally, MS/HS sensor has larger number and narrower width of spectral bands which only collect specific narrow spectrum of energy leading to a lower image Signal to Noise Ratio (SNR). For the purpose of maintaining a relatively good image SNR and balancing the tradeoff [2] between the spectral and spatial resolution quality, the MS/HS sensor is designed with a larger IFOV to collect more light and this causes a lower spatial quality. However, in contrast, PAN sensor with a single wider band in the visible spectrum has a smaller IFOV which generates relatively good spatial resolution image [2].

(2) The high spatial quality MS/HS image data volume is greatly large [2]. Compared to the bundled poor spatial quality MS/HS image with a higher spatial quality PAN image data volume, the high spatial quality MS/HS image data volume is significantly larger which can result in a big problem of limited data storage capacity on board and bandwidth transmission from platform to ground receiver [3].

Considering these constraints, an image fusion technique which can fuse together the observed poor spatial quality MS/HS image and a higher spatial quality PAN image to generate a corresponding high spatial quality MS/HS image, is necessary to satisfy the practical utilizations of satellite images. In this fusing process, spatial composition of panchromatic image and spectral composition of MS/HS image ought to be preserved as completely as possible so that the final estimated image can provide both spatial and spectral details of observed images as much as possible. The fusion technique is the well-known pansharpening.

Pansharpening aims at taking advantage of both the geometric spatial structures of panchromatic image and the spectral composition of MS/HS image to generate a fused high spatial quality MS/HS image. Such synthetic images are in high demand in some commercial applications like Bing Maps and Google Earth [4]. Pansharpening is also a crucial pre-processing stage for some other satellite imagery based applications, for example in scene interpretation [5], object recognition [6], classification [7] and change detection [8]. Figure 1.2 shows the principle of pansharpening process.

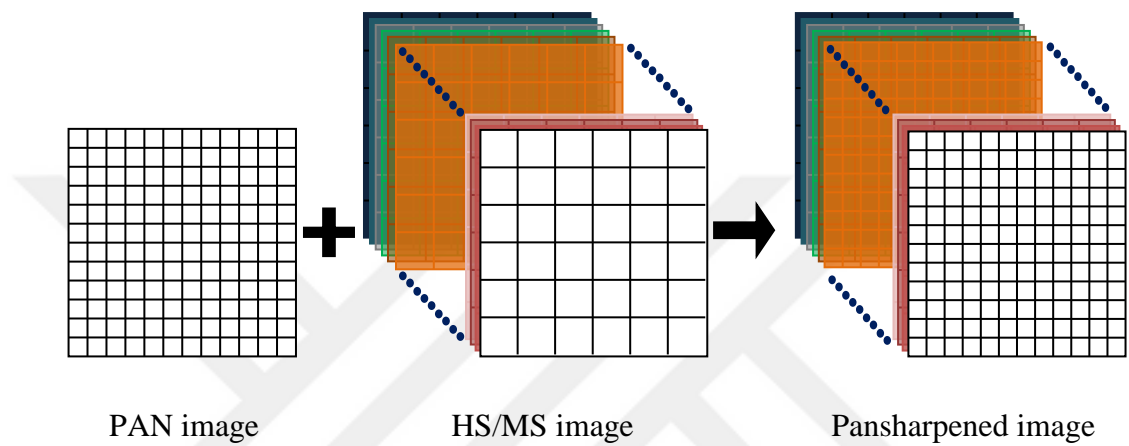


Figure 1.2: Basic principle of Pansharpening process.

1.1 Purpose of Thesis

This thesis research firstly gives a general classification of various pansharpening methods which can be utilized for both MS images and HS images. In recent years, many improved conventional or newly proposed pansharpening methods have emerged. The differences and similarities among different methods need to be clearly noted and studied. This thesis generally classifies the pansharpening approaches into three groups: the Component Substitution (CS) category, the Multi-Resolution Analysis (MRA) category and the model based category.

Another purpose of the thesis is to improve a model based pansharpening method by using a proposed Guiding Image Block-Matching 3D (GIBM3D) denoising algorithm. Different MS and HS datasets are tested and compared under the proposed model. Experiments also give competitive results of the proposed model.

1.2 Outline of Thesis

The thesis contains five chapters. A brief introduction of the pansharpening technique background including its applications and some technical constraints is given in Chapter 1.

In Chapter 2, an overview of different pansharpening methods are presented and a general classification for these methods is summarized as follows: CS category, MRA category and the model based category. Then, some important representative pansharpening methods are discussed and compared.

In Chapter 3, the BM3D denoising algorithm is firstly introduced and based on this the Guiding Image BM3D (GIBM3D) denoising algorithm is proposed. Then a model based pansharpening method is presented in detail, where the GIBM3D is used inside an ADMM based pansharpening algorithm. The resulting newly proposed ADMM-GIBM3D pansharpening method is explained in detail.

In Chapter 4, the proposed ADMM-GIBM3D pansharpening method and some selective representative methods are implemented on five different image datasets. Then, the experimental results are displayed and compared in the following sections.

Finally, Chapter 5 concludes this thesis and presents possible subsequent work for the proposed GIBM3D denoising algorithm.

2. OVERVIEW OF PANSHARPENING METHODS

With the development of pansharpening techniques, many researchers are trying to give a renewed set of classification categories for various pansharpening methods.

In [9, 10], pansharpening methods are broadly grouped into two groups: basic CS category methods and MRA category methods. In [11], pansharpening methods are classified into CS group, MRA group and regularization based methods. They formulate an image formation model from the final estimated MS image to the low-resolution quality MS and PAN observation images according to the compressed sensing theory [11]. Using sparse regularization, the high spatial quality MS image can be restored from its degraded versions. In [12], pansharpening methods are grouped into CS class, MRA class and Bayesian class which is a particular case for variational methods. The Bayesian method is used to deal with an inverse problem via the posterior distribution in the Bayesian framework model [12]. In [13], pansharpening methods are classified into four classes: CS class, MRA class, model based class and sparse reconstruction (SR) class. They group the methods which build a relationship model between targeted image and the observed images as an ill-posed problem into the model based class. In [3], pansharpening methods are classified into CS group, MRA group and variation optimization based group. In [2], [14], pansharpening methods are classified into four classes: CS class, MRA class, hybrid class and model based class. In terms of Hybrid class, it combines the advantages of both CS class and MRA class, and it can be regarded as an improved version of CS class or MRA class. They also group the compressive sensing methods, the sparse representation methods and the Bayesian fusion into the model based methods. CS and MRA family are the most popular and well-known pansharpening methods. Meanwhile there are many other existing pansharpening methods which are derivative versions of Bayesian framework [15] methods, sparse representation methods [16, 17], variational optimization [18–20] methods. They are based on some specific theoretical image

models [16]. Therefore, they can be roughly summarized as the model based methods. In recent years, many different effective deep-learning (DL) based methods like convolutional neural network (CNN) [21] and generative adversarial network (GAN) [22] have been introduced into the pansharpening area. In [23], a three-layer architecture Convolutional Neural Network based pansharpening method is proposed. In [24], a Deep Residual Network (DRN) is proposed to fully utilize the high non-linearity of DL model. In [22], a Generative Adversarial Network (GAN) pansharpening method is proposed with a generator of two-stream fusion architecture and a discriminator of fully convolutional network.

In this thesis based on the previous discussion as shown in Table 2.1, various traditional pansharpening methods will be grouped into CS category, MRA category and model based category with a new DL based category. Such classification of pansharpening methods can contribute to easier and clearer comparisons among different pansharpening categories.

Table 2.1: Different categories of pansharpening methods.

Category	Method	References
CS	PCA/GFPCA	[25, 26]
	GS/GSA	[27, 28]
MRA	SFIM	[29]
	HPF	[30]
	MTF-GLP	[31, 32]
Model based	variational model	[18, 33]
	compressive sensing based	[11]
DL based	CNN/GAN/DRN	[21, 22-24]

2.1 Component Substitution (CS) category

CS based pansharpening methods are important and widely used in some commercial remote sensing software like ERDAS, ENVI, ESRI and PCI due to its less time consumption, simplicity and good performance [3].

The CS family substitutes the low-resolution spatial (structural) composition of MS/HS image by using the higher-resolution spatial composition of PAN image. The process can be found in Figure 2.1 as a diagram. The high-resolution spatial

information is generated by subtracting the combined low-resolution spatial composition of MS/HS image from the PAN image.

The CS family approaches differ in how to get the substituted low-resolution spatial composition of MS/HS image by separating the spatial and spectral compositions. They also differ by how much high-resolution information is added into the MS/HS image, which is how much gain is multiplied by the injected high-resolution details [3]. This general notion can be presented as:

$$\hat{H} = \tilde{H} + g(P - I_L) \quad (2.1)$$

In Eq. 2.1 and in Figure 2.1, \hat{H} is the final target MS/HS image, \tilde{H} is the resampled pan-scale MS/HS image, g represents the gain values of injected high-resolution information, P is normalized PAN image. I_L is combined low-resolution component from MS/HS image [3].

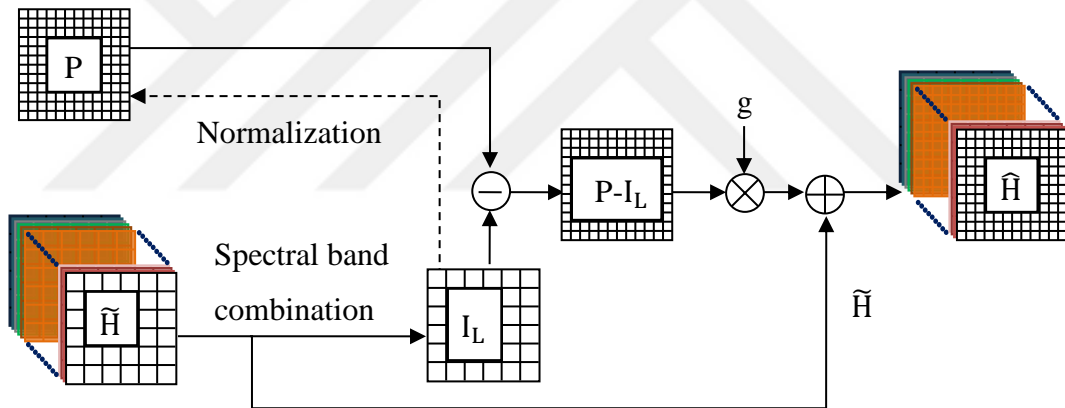


Figure 2.1: Pansharpener flowchart of CS family.

Various CS family methods try to optimize the composition of the I_L and the gain g . The correlation of I_L and PAN image determines the distortion degree of final estimated image. The greater the correlation, the smaller is the distortion. Histogram matching must be performed before the substitution process is executed. This ensures that similar statistical characteristics (mean and variance value) for the PAN images and the substituted compositions [2].

Gram-Schmidt (GS) method has become a popular CS-based pan-sharpening methods since it was published in 1998 [27]. The flowchart of GS approach is shown in Figure 2.2. In GS, I_L is generated as given in Eq. (2.2) with equal weights $\frac{1}{N}$ along the spectral dimension.

$$I_L = \left(\frac{1}{N}\right) \sum_1^N \tilde{H} \quad (2.2)$$

Here, N denotes the total number of bands in MS/HS image.

Gain g is a vector $g=[g_1, g_2 \dots g_N]$ which equals the ratio of the covariance matrix of pan-scale \tilde{H} with synthesized low-resolution information I_L , to the variance of the synthesized low-resolution information I_L . This is calculated as follows:

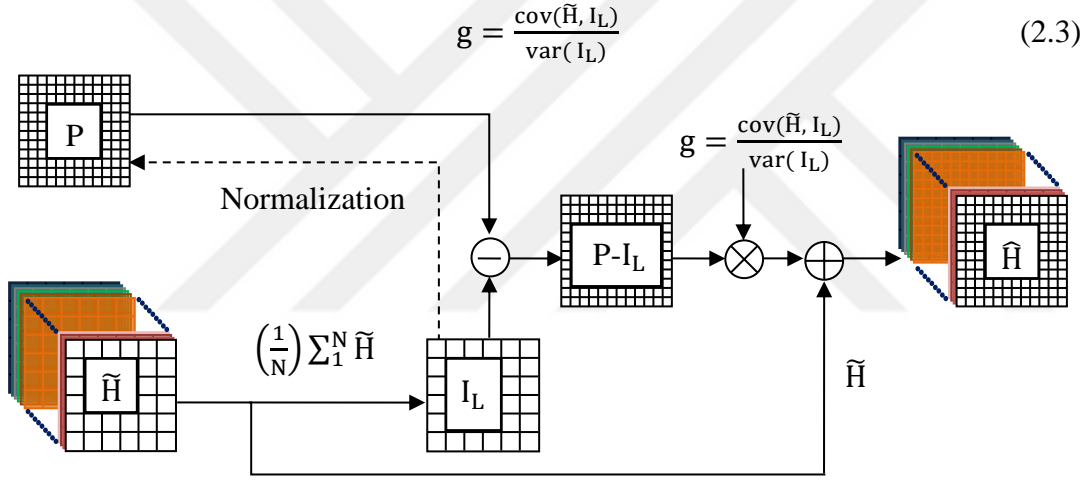


Figure 2.2: Pansharpening flowchart of GS method.

An improved version of GS method is GS Adaptive (GSA) [28]. In GSA method the weights for synthesizing I_L are determined by minimizing mean square errors of the downsampled MS/HS-scale pan image \tilde{P} and the low-resolution information,

$$\tilde{I}_L = \sum_{i=1}^N w_i \cdot \hat{H}_i, (w_i = \hat{H}_i \setminus \tilde{P}) \quad (2.4)$$

Then, the obtained weights are applied to generate the pan-scale low-resolution information:

$$I_L = \sum_{i=1}^N \tilde{w}_i \cdot \tilde{H} \quad (2.5)$$

Another important CS based pansharpening method is Principal Component Analysis (PCA) method [25]. It assumes the first PC of MS/HS image contains almost all low-resolution spatial composition and the others contain spectral composition. Therefore, the first PC is substituted by PAN image, followed by inverse PCA algorithm to generate the target image.

PCA pansharpening method can be implemented fast, and it can keep the spatial structure well. However, it has the serious shortcoming of spectral distortion. In [26], a Guided Filter (GF) PCA as shown in Figure 2.3 was proposed, assuming that the first $i \ll n$ PCs contain most information and the remaining $(n-i)$ PCs mainly contain noise information. Before the inverse PCA is implemented, a GF is applied to the first i PCs. The guided PAN image is also used together with the GF to preserve the spatial structure composition, and denoising is applied to the residual PCs. Compared to the simple PCA algorithm, GFPCA can preserve spectral information better, however it introduces serious spatial blur. In this sense, GFPCA is not only a CS based method, but also an MRA based method which will be reviewed next.

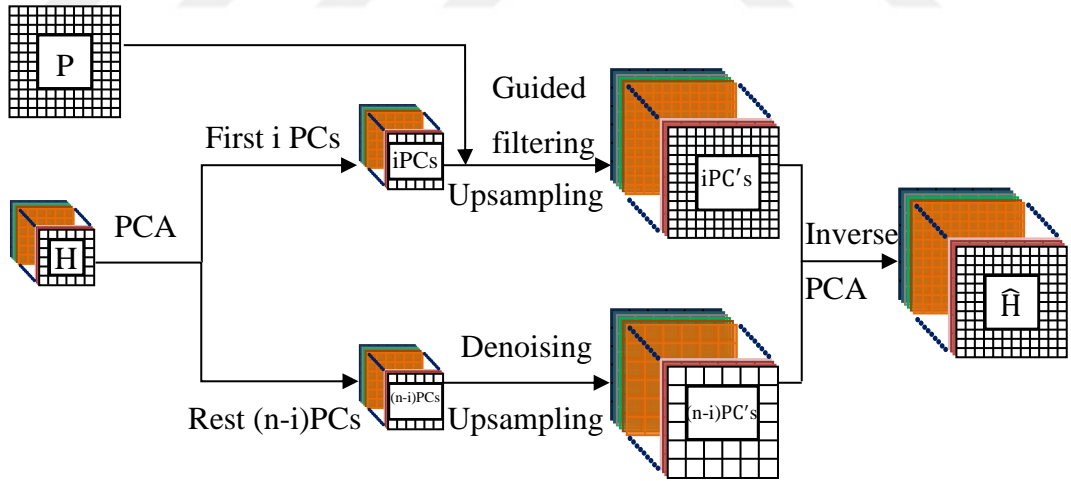


Figure 2.3: Pansharpening flowchart of GFPCA method.

2.2 Multiresolution Analysis (MRA) category

The Multiresolution Analysis (MRA) family usually utilizes some spatial filters on PAN image to yield spatial structure details added into the MS/HS images to derive pansharpened MS/HS images. The details for MRA approach are shown in Figure 2.4. Compared to CS family methods with composite low spatial resolution term I_L from the MS/HS image which always leads to significant spectral distortions, MRA family approaches always apply some low-pass filters to generate I_L term from PAN image. Thus, MRA family has a better spectral consistency. However, because of the design of the fitting filters, the complexity and calculation time for this family of methods are increased when compared to CS family [34].

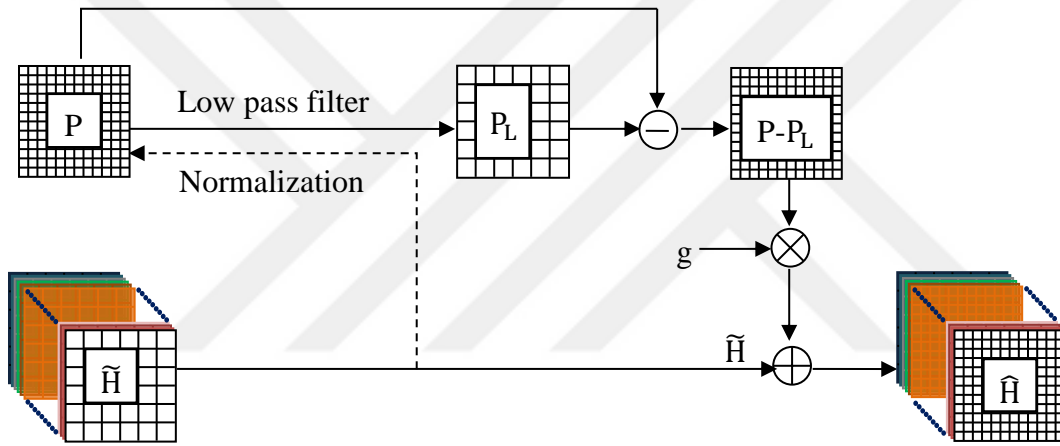


Figure 2.4: Pansharpener flowchart of MRA family.

The MRA methods differ in how they obtain the low-resolution information P_L that is generated from the PAN image P and how much weight of details needs to be injected to the MS/HS images. The pansharpener process is summarized as follows:

$$\hat{H} = \tilde{H} + g(P - P_L) \quad (2.6)$$

\hat{H} is the final target MS/HS image. \tilde{H} represents resampled MS/HS image. And g denotes gain values. P represents normalized PAN image. P_L is different from the I_L of CS family methods. It represents low-pass composition of PAN image.

In [30], a High Pass Filter (HPF) is directly used to collect high quality spatial component from PAN image which is denoted by $(P - P_L)$.

The Smoothing Filter-based Intensity Modulation (SFIM) [29] method utilizes low-pass filter to generate the low-resolution information P_L . The gain g equals the ratio of each band of \tilde{H} and low-resolution component P_L . As shown in Figure 2.5, these steps are given as follows:

$$g = \frac{\tilde{H}}{P_L} \quad (2.7)$$

$$P_L = P * h_{LP} \quad (2.8)$$

$$\hat{H} = \tilde{H} + \frac{\tilde{H}}{P_L} (P - P * h_{LP}) \quad (2.9)$$

The resulting equation is as given below.

$$\hat{H} = \frac{\tilde{H}}{P_L} P \quad (2.10)$$

h_{LP} is a low-pass filter (e.g. an averaging filter). Gain g is calculated on each single band of HS image.

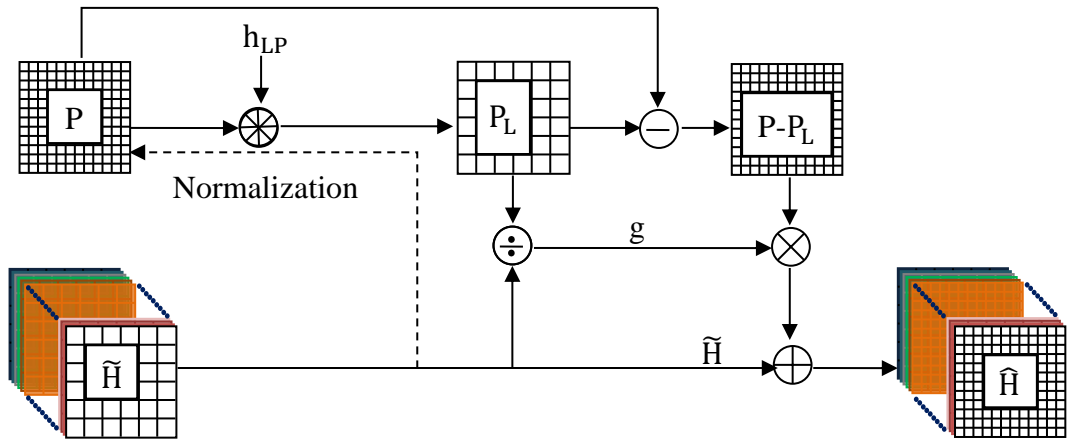


Figure 2.5: Pansharpening flowchart of the SFIM method.

In [31, 32] The Generalized Laplacian Pyramid (GLP) methods utilizing modulation transfer function (MTF) apply Gaussian filters on pan image to obtain a Gaussian

pyramid. In some Gaussian pyramidal methods, they also calculate gain by the ratio of the covariance of \tilde{H} with the low-passed P_L and the variance of P_L , which is $g = \frac{\text{cov}(\tilde{H}, P_L)}{\text{var}(P_L)}$.

2.3 Model based category

Another important category for pansharpening methods is model based family of pansharpening algorithms. As shown in Figure 2.6, model based family usually builds a relationship model from the final estimated image to the observed MS/HS and PAN images.

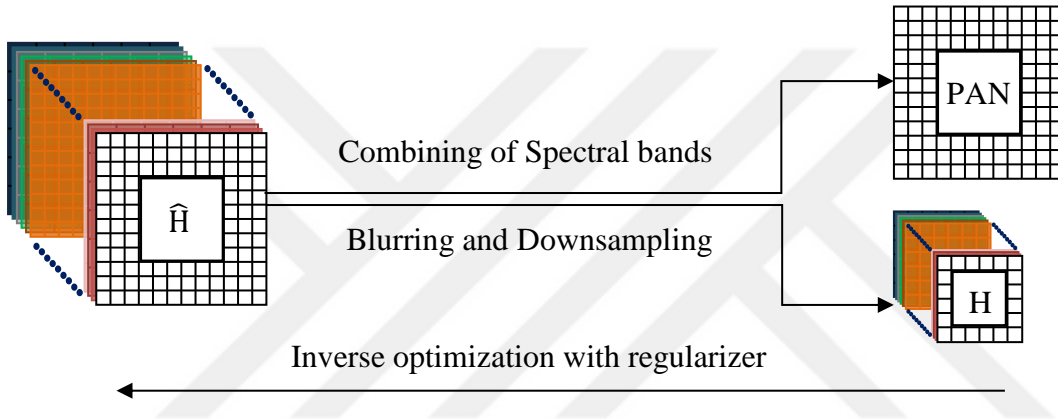


Figure 2.6: Pansharpening flowchart of Model based family.

This observation model based fusion process is regarded as an inverse problem which generally has three constraining terms: PAN constraint term, spectral constraint term and regularization constraint term. The first two terms constrain the target pansharpened image to be consistent with the observed images. The third regularization term can impose image model constraints using different priors [3]. These different regularization terms include total variation (TV) prior [35], Huber-Markov prior [36], nonlocal prior [18], and other possible regularizers [3]. The general observation model for the pansharpening problem in a model based setting is expressed as follows [3]:

$$E(z) = \lambda_1 \|\alpha_1(z) - \text{PAN}\| + \lambda_2 \|\alpha_2(z) - z^\Omega\| + \lambda_3 p(z) \quad (2.11)$$

Here, z represents the target estimate, z^Ω represents resampled MS/HS image, λ_1, λ_2 and λ_3 represent the balance factors among the three terms. α_1 and α_2 represent the imaging formation operations denoting how the observed images are formed from the target image z . $\|\cdot\|$ represents norm calculations on the discrete multichannel data. $p(z)$ denotes different priors used for regularization, such as TV or wavelet sparsity.

Bayesian inference model is a good way to tackle the inverse problem of solving Eq. (2.11) for z . In [15], in the Bayesian estimation model, the operators $\alpha_1(\cdot)$ and $\alpha_2(\cdot)$ have been chosen to represent blurring or subsampling operations. Next, a Monte Carlo algorithm based on Markov chains is used to optimize the model function. In [37], the operators $\alpha_1(\cdot), \alpha_2(\cdot)$ and the prior $p(\cdot)$ are constructed by using the multi-order gradients which obey the Gaussian distribution. Then, an ADMM [38] algorithm is applied to minimize the energy equation Eq. (2.11).

In [18, 33], a variational model is proposed by assuming that the geometric composition of MS/HS image is included in the corresponding PAN image. PAN should be produced by linearly combining different channels from MS/HS image with mixing coefficients which correspond to α_1 . z^Ω is related to target pansharpened image z by firstly using low-pass filter and then subsampling which can now be represented by α_2 . The prior utilized is variational regularization or nonlocal regularization. In [18, 33], they use iterative optimization method or gradient descent method to optimize the energy function Eq. (2.11) to get to the target image.

In [11] compressed sensing (CS) theory based pansharpening method is proposed. This theory assures that the final estimate x can be properly reconstructed from the noisy image y under sparse regularization.

$$\hat{\alpha} = \arg \min \|\alpha\|_0 \quad \text{subject to } \|y - \Phi\alpha\|_2^2 \leq \varepsilon \quad (2.12)$$

Here, $\|\alpha\|_0$ represents the number of nonzero elements in α . Φ denotes basis elements which form a dictionary. ε is the reconstruction error. α is the sparse representation of x using the atoms of dictionary Φ [39]. The estimated x can be calculated by $x = \Phi\hat{\alpha}$.

Model based pansharpening methods are being rapidly developed with the introduction of new models. Compared to the CS family and MRA family, model based pansharpening family has less spatial and spectral distortion [12]. However, owing to the complexity and large amount of calculation, model based family generally consumes more time and computational resources compared to CS family and MRA family pansharpening methods.



3. SPARSITY BASED PANSHARPENING

Sparse representation in recent years has attracted considerable interests in image restoration [40, 41], image denoising [42] and image superresolution [43]. As shown in Figure 3.1 sparse representation assumes that for “well-behaved” natural images neighboring pixels have strong correlation [39]. Hence, natural images can be sparsely represented over some basis elements set such as an overcomplete dictionary.

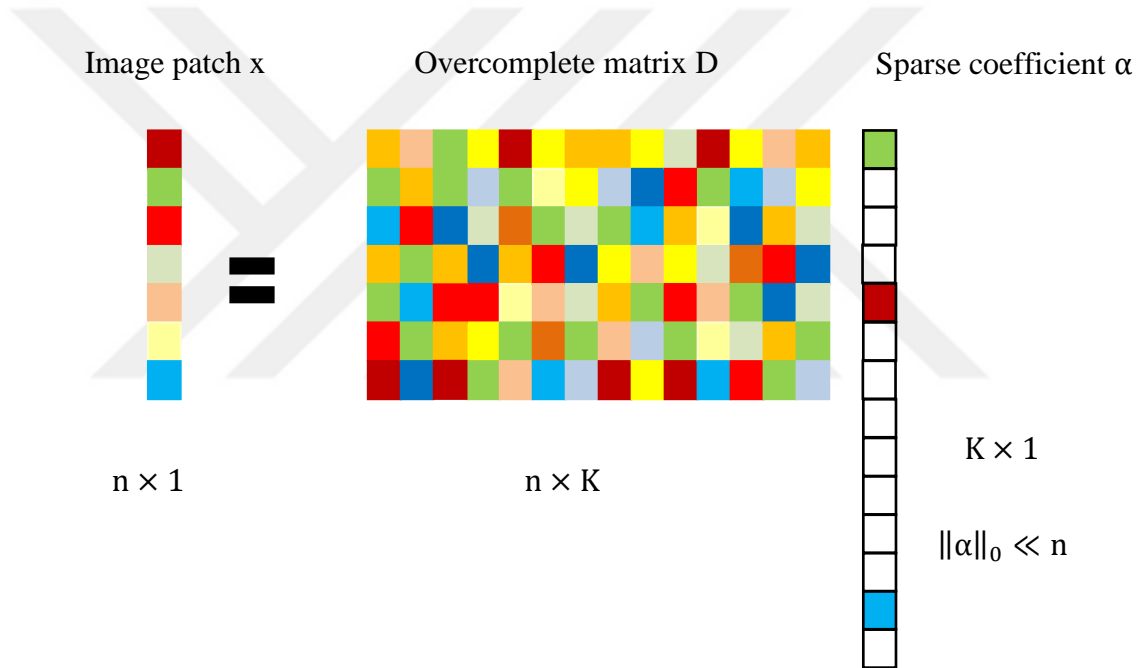


Figure 3.1: Principle of sparse representation.

Sparse representation theory supposes that for any image $x \in \mathbb{R}^n$, there exists a matrix $D \in \mathbb{R}^{n \times K}$ called as a dictionary, which contains K prototype base elements, also referred to as atoms. The image x can be expressed approximately by linearly combining atom images in D , that is $x = D\alpha$. Here, $n < K$, hence D forms a dictionary which allows redundancy in describing x [41]. α is the sparse coefficient vector. α has many possible values. The sparse representation problem is to find a α which has as few nonzero components as possible [11]. It is defined as follows:

$$\hat{\alpha} = \arg \min \|\alpha\|_0 \quad \text{s. t. } \|D\alpha - x\|_2^2 = 0 \quad (3.1)$$

where $\|\alpha\|_0$ represents the number of nonzero elements in α .

Practically, we only observe a part of measurements y of x [11],

$$y = Lx = LD\alpha \quad (3.2)$$

where $L \in \mathbb{R}^{m \times n}$ ($m < n$) denotes the encoding process of CS theory [44]. x can be properly reconstructed from the noisy image y with

$$\hat{\alpha} = \arg \min \|\alpha\|_0 \quad \text{subject to } \|y - LD\alpha\|_2^2 \leq \varepsilon \quad (3.3)$$

The denoised or reconstructed image \hat{x} can be recovered by $\hat{x} = LD\hat{\alpha}$.

3.1 BM3D image model

Block-matching 3-D (BM3D) image model is based on overcomplete sparse representation. It was first introduced in image denoising [45] with exciting results, and its efficient performance has been utilized in image deblurring [46], superresolution [47] and image reconstruction [48]. BM3D algorithm groups similar 2D image blocks (image patches) into 3D block cubes as shown in Figure 3.2 to enhance the sparsity in transform domain. In this thesis, BM3D is used as a regularizer to solve a model based pansharpening problem. BM3D as a denoising regularizer is implemented in every iteration of an iterative process to enhance the pansharpening performance.

In [49], the BM3D analysis and synthesis framework is introduced in detail, and the complicated BM3D analysis framework is summarized as a multiplication by a single matrix forming a nontight frame [48] as follows:

$$\omega = \Phi x \quad (3.4)$$

Here, $x \in \mathbb{C}^N$ is the vectorized noisy image. $\omega \in \mathbb{C}^M$ stores 3-D group spectrum coefficients and is called as joint 3-D groupwise spectrum. Matrix Φ represents the BM3D analysis operation. The blocks which are similar to the reference blocks (i.e.

currently processed one) are stacked together into a 3D group (array) according to some similarity criterion. Since each pixel may be located in different blocks due to the similarity, blocks can cover each other and the pixel number in the 3D cube is much greater than the one in the actual image [49]. Hence, $\Phi \in \mathbb{C}^{M \times N}$ with $M \gg N$ in fact implements an overcomplete sparsity transform into the 3D space [48].

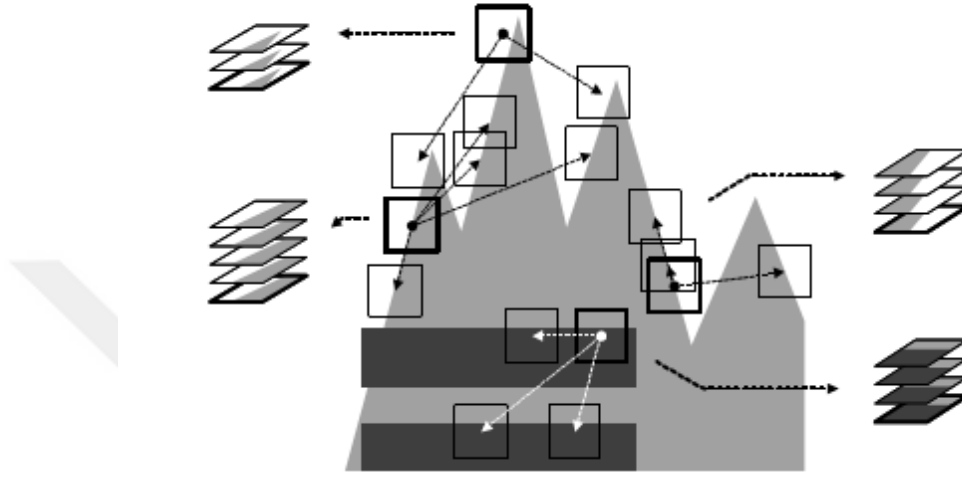


Figure 3.2: Block-matching of patches into 3D array according to similarity (reference block with thick borders) [45].

The denoising process of BM3D algorithm is shown in Figure 3.3. In the 3D transform space, collaborative filtering such as hard-thresholding filtering or Wiener filtering performs a denoising strategy on formed groups. Then, inverse 3D transform is implemented on all the blocked groups, and the denoised image blocks are transformed back to the original positions by averaging all the obtained denoised image blocks with weights due to their overlapping [45, 49]. This inverse transform process is depicted as

$$x = \psi\omega \quad (3.5)$$

$\psi \in \mathbb{C}^{M \times N}$ in [49] denotes the synthesis frame [48]. Both Φ and ψ employ the 3D transform which is combined with 2-D intrablock transforms and cube transforms [49]. This combination of transforms efficiently improves the approximation of spectral image [49], makes use of the 3D block cube structure and cuts down the computational complexity greatly compared with a 2-D blockwise transform [48].

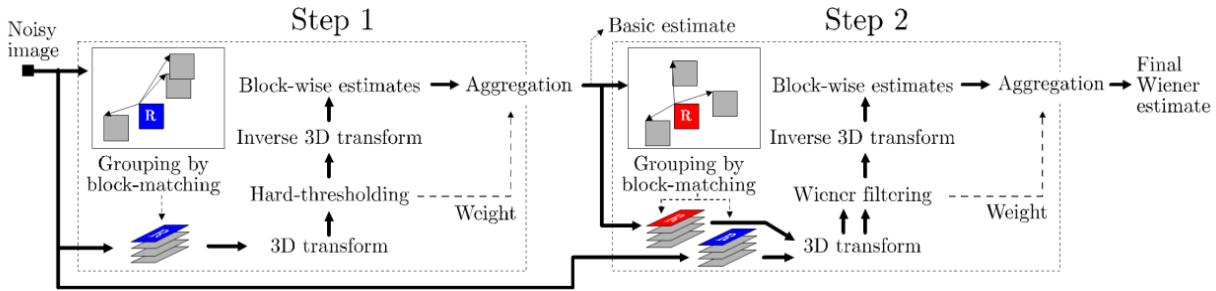


Figure 3.3: Flowchart of the BM3D denoising algorithm [45].

3.2 Proposed Guiding-Image-BM3D model

There are two main steps in the original BM3D model as shown in Figure 3.4. The first step is implemented with a hard-thresholding filter to remove the noise, and we call the first step the “Hard-thresholding step” for simplicity. The result of the Hard-thresholding step is the basic image estimate, and this is one of the two inputs of the second step. In the second step, the Wiener filter is implemented using two 3D transformed inputs, where the inputs are the basic estimate and the noisy image. We call the second step as the Wiener filtering step for simplicity. The basic estimate here is mainly used to enhance grouping performance of block-matching in the Wiener filtering step. Secondly it acts as the pilot signal to determine the Wiener shrinkage coefficients for the 3D energy spectrum [45]. In some sense, the basic estimate acts as a reference for better grouping and coefficient calculation in the Wiener filtering step.

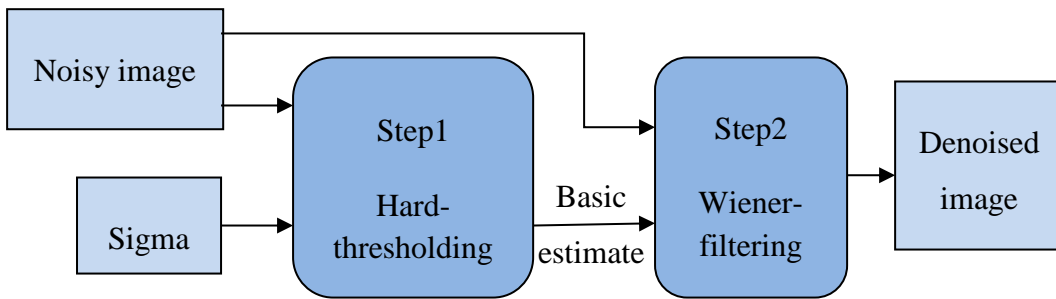


Figure 3.4: Simplified flowchart of the BM3D denoising algorithm.

In this thesis, a new Guiding Image BM3D (GIBM3D) model (Figure 3.5) is proposed to enhance the performance of pansharpening methods which utilize denoising as a substep of an iterative pansharpening method.

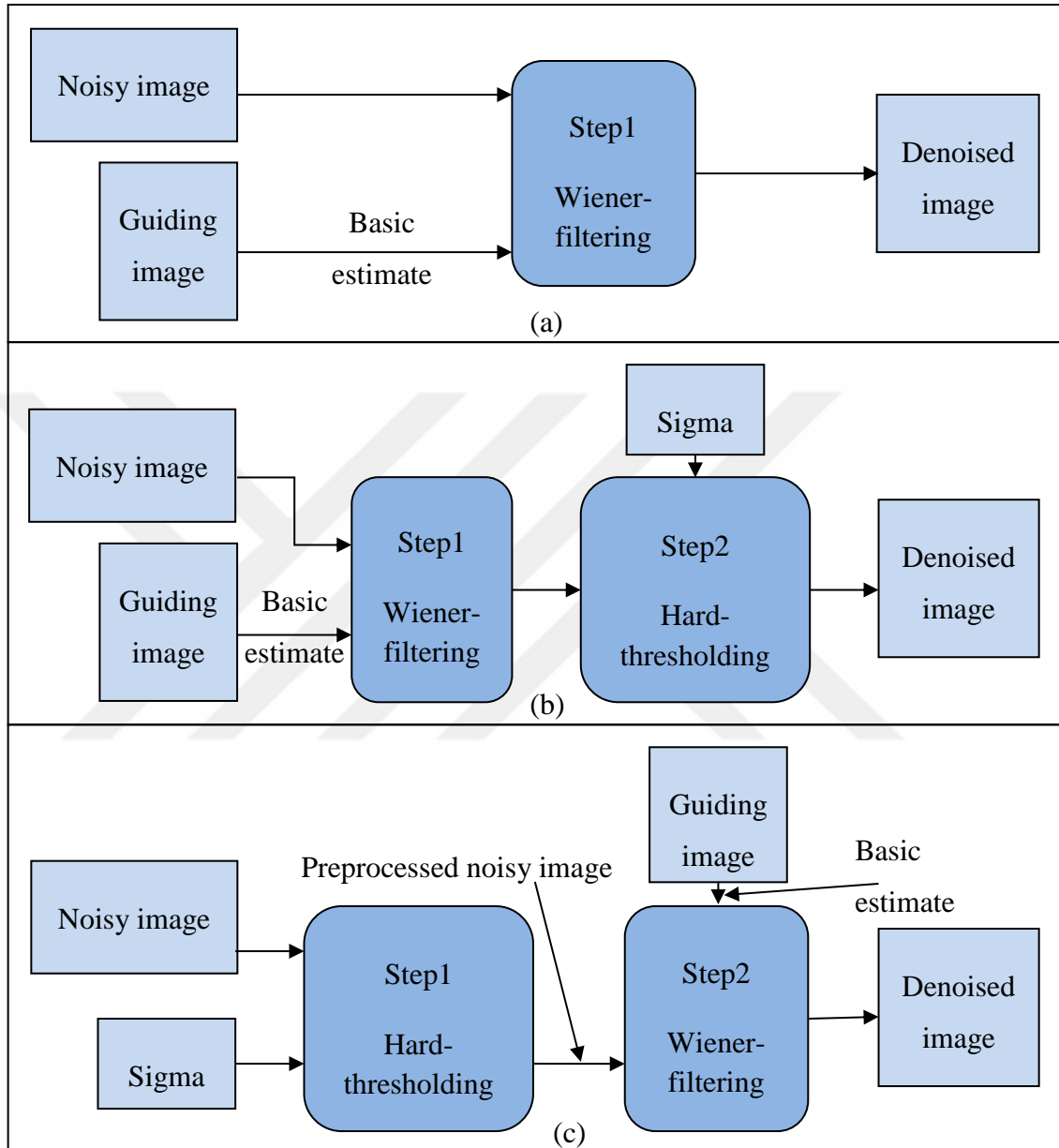


Figure 3.5: Flowchart of proposed GIBM3D denoising algorithm. (a) GIBM3D-w sub-model, (b) GIBM3D-wth sub-model, (c) GIBM3D-thw sub-model.

In the Guiding Image BM3D approach proposed in this thesis, the essential idea is to replace the basic estimate input of the Wiener filtering step with an external guiding image.

With this idea, there are three main sub-GIBM3D-models which can be generated. The first sub-model (GIBM3D-w in Figure 3.5a) uses a single Wiener filtering step with two inputs, where one input is the external guiding image acting as a basic estimate and the second input is the noisy image. The second sub-model (GIBM3D-wth in Figure 3.5b) adds the thresholding step after the first sub-model GIBM3D-w. Hence, the output of the first sub-model is further processed in the subsequent Hard-thresholding step using a proper sigma value. The third sub-model (GIBM3D-thw in Figure 3.5c) adds a thresholding step before the first sub-model GIBM3D-w. This way, the Hard-thresholding step with a proper sigma produces the preprocessed noisy image, and this preprocessed noisy image and a guiding external image form the two inputs of the secondary guiding-image based Wiener filtering step.

3.3 HySure: A model based pansharpening method

In Section 2.3, the general model based pansharpening framework has been introduced using the energy formula $E(z)=\lambda_1\|\alpha_1z - \text{PAN}\|+\lambda_2\|\alpha_2z - z^\Omega\| +\lambda_3 p(z)$. Here, a more detailed energy function will be presented.

Let $Y_h \in \mathbb{R}^{L_h \times n_h}$ represent the observed MS/HS image. Assume it has L_h bands and n_h pixels in each band. Let $Y_p \in \mathbb{R}^{L_p \times n_p}$ ($L_h > L_p$ and $n_p > n_h$) represent the given PAN image, and assume it has L_p spectral bands and n_p pixels. Let $Z \in \mathbb{R}^{L_h \times n_p}$ denote the final estimated high spatial quality MS/HS image, and assume it has L_h spectral bands and n_p pixels. The inverse imaging model can be presented as follows:

$$Y_h = Z\alpha_1 + N_h \quad (3.6)$$

$$Y_p = \alpha_2 Z + N_p \quad (3.7)$$

Here, α_1 and α_2 denote how the observed images are formed from the estimated MS/HS image, respectively. In general we can assume that α_1 represents the process of blurring and subsampling, and α_2 denotes spectral responses of sensor. Hence $\alpha_1 = \text{BM}$ and $\alpha_2 = \text{R}$, where $\text{B} \in \mathbb{R}^{n_p \times n_p}$ is the blurring matrix, $\text{M} \in \mathbb{R}^{n_p \times n_h}$ is subsampling operator and $\text{R} \in \mathbb{R}^{L_p \times L_h}$ is spectral response matrix. Matrix B and R are assumed to

be known, and they can also be estimated from the data [19]. N_h and N_p denote independent and identically distributed (i.i.d.) noises. Estimating Z depicts an inverse problem which can be tackled by applying a variational formulation. Therefore the estimated image \hat{Z} is the solution of the following optimization function:

$$\hat{Z} \in \arg \min_Z \frac{1}{2} \|Y_h - ZBM\|_F^2 + \frac{\lambda_p}{2} \|Y_p - RZ\|_F^2 + \lambda_\varphi \varphi(Z) \quad (3.8)$$

Here, $\|\cdot\|_F^2$ denotes squared ℓ_2 norm and φ is a regularizer function.

Considering the considerably large volume of the hyperspectral image data, [19] proposed to translate the data representation into a subspace having a relatively lower dimension due to the large correlation among different spectral bands [50]. The spectral vector of size L_h tends actually to live in a subspace of dimension L_s , with $L_s \ll L_h$. Let $E \in \mathbb{R}^{L_h \times L_s}$ represent a basis of an identified subspace. The high dimensional image Z can be expressed as $Z=EX$, and here $X \in \mathbb{R}^{L_s \times n_p}$ with much lower dimension will be estimated instead of Z . $E \in \mathbb{R}^{L_h \times L_s}$ can be identified through some existing methods like VCA [51], PCA and singular value decomposition (SVD).

With above transformation, the optimization function can be written as follows:

$$\hat{X} \in \arg \min_X \frac{1}{2} \|Y_h - EXBM\|_F^2 + \frac{\lambda_p}{2} \|Y_p - REX\|_F^2 + \lambda_\varphi \varphi(X) \quad (3.9)$$

The first two terms are observation fidelity terms, which preserve the spatial and spectral information. The third term imposes constraint or prior.

To solve the optimization function, a Split Augmented Lagrangian Shrinkage (SALSA) algorithm [52] is used in [19] as an example of ADMM. Firstly, the optimization variable X is splitted into four new variables: a new X that actually equals to the original X with three auxiliary variables V_1 , V_2 and V_3 . Thus, the new optimization problem is as follows:

$$\hat{X}, \hat{V}_1, \hat{V}_2, \hat{V}_3 \in \arg \min_{X, V_1, V_2, V_3} \frac{1}{2} \|Y_h - EV_1M\|_F^2 + \frac{\lambda_p}{2} \|Y_p - REV_2\|_F^2 + \lambda_\varphi \varphi(V_3)$$

$$\text{subject to } V_1 = XB, V_2 = X, V_3 = X \quad (3.10)$$

The augmented Lagrangian [53] of above problem can be given as follows:

$$\begin{aligned} \mathcal{L}(X, V, D) = & \frac{1}{2} \|Y_h - EV_1 M\|_F^2 + \frac{\lambda_p}{2} \|Y_p - REV_2\|_F^2 + \lambda_\varphi \varphi(V_3) \\ & + \frac{\mu}{2} (\|XB - V_1 - D_1\|_F^2 + \|X - V_2 - D_2\|_F^2 + \|X - V_3 - D_3\|_F^2) \end{aligned} \quad (3.11)$$

Here, $D = (D_1, D_2, D_3)$ is the Lagrange multiplier, also called as a dual variable [38]. μ is the penalty parameter.

The solution to this optimization problem is first to keep V as a constant while solving a minimization function for X . Then X is kept as constant while solving a minimization function for V . For the different V terms, the same minimization strategy is used. Hence, all the terms not to be solved are kept as constants, while the minimization function is solved with respect to one of them. After the minimization steps, all the dual variables are updated. The detailed solving process is given in the following section.

Minimize function for one variable while keeping others fixed:

$$X^{k+1} = \arg \min_X \|XB - V_1 - D_1\|_F^2 + \|X - V_2 - D_2\|_F^2 + \|X - V_3 - D_3\|_F^2, \quad (3.12)$$

$$V_1^{k+1} = \arg \min_{V_1} \frac{1}{2} \|Y_h - EV_1 M\|_F^2 + \frac{\mu}{2} \|X^{k+1} B - V_1 - D_1^k\|_F^2, \quad (3.13)$$

$$V_2^{k+1} = \arg \min_{V_2} \frac{\lambda_p}{2} \|Y_p - REV_2\|_F^2 + \frac{\mu}{2} \|X^{k+1} - V_2 - D_2^k\|_F^2, \quad (3.14)$$

$$V_3^{k+1} = \arg \min_{V_3} \lambda_\varphi \varphi(V_3) + \frac{\mu}{2} \|X^{k+1} - V_3 - D_3^k\|_F^2, \quad (3.15)$$

Update Lagrange multipliers:

$$D_1^{k+1} = D_1^k + V_1^{k+1} - X^{k+1} B, \quad (3.16)$$

$$D_2^{k+1} = D_2^k + V_2^{k+1} - X^{k+1}, \quad (3.17)$$

$$D_3^{k+1} = D_3^k + V_3^{k+1} - X^{k+1}. \quad (3.18)$$

Above calculating process is repeated until specific criteria is satisfied. The minimization regarding X , V_1 and V_2 are quadratic problems, and they can be solved by using FFT [19]. Following [19], the respective solutions of the first three minimization functions Eq.(3.12) to Eq.(3.14) are given as follows:

$$X^{k+1} = [(V_1^k + D_1^k)B^T + (V_2^k + D_2^k) + (V_3^k + D_3^k)][BB^T + 2I]^{-1}, \quad (3.19)$$

$$V_1^{k+1} = [EE^T + \mu I]^{-1}[E^T Y_h + \mu(X^{k+1}B - D_1^k)] \odot M \\ + (X^{k+1}B - D_1^k) \odot (1 - M), \quad (3.20)$$

$$V_2^{k+1} = [\lambda_p E^T R^T R E + \mu I]^{-1}[\lambda_p E^T R^T Y_p + \mu(X^{k+1} - D_2^k)]. \quad (3.21)$$

As for Eq. (3.15), its solution is dependent on the choice of regularizer term φ . In [19], a vector total variation (VTV) prior is utilized as the regularizer.

$$\varphi(X) \stackrel{\text{def}}{=} \sum_{c=1}^{n_p} \sqrt{\sum_{r=1}^{L_s} \{[(XD_h)_{rc}]^2 + [(XD_v)_{rc}]^2\}} \quad (3.22)$$

Here, r and c represent row and column indices, respectively. D_h and D_v help to calculate row differential and column differential of the image. Therefore, V_3 is splitted into two variables XD_h and XD_v . Hence, the fourth function becomes as follows:

$$[V_3^{k+1}, V_4^{k+1}] = \arg \min_{V_3, V_4} \lambda_\varphi \varphi(V_3, V_4) + \frac{\mu}{2} \|X^{k+1}D_h - V_3 - D_3^k\|_F^2 \\ + \frac{\mu}{2} \|X^{k+1}D_v - V_4 - D_4^k\|_F^2 \quad (3.23)$$

The Eq. (3.23) can be solved with vector-soft thresholding function [19].

Actually, the regularizer term φ can be replaced by any state of the art denoisers.

3.4 Proposed ADMM-GIBM3D pansharpener method

In the iterations of ADMM, the estimate function is decoupled to the prior term and forward model terms [54]. This modular structure [55] is an important feature for ADMM algorithm. The first three forward imaging terms, Eq. (3.12) to Eq.(3.14), can be treated as inversion steps. The regularization term Eq.(3.15) can be treated as a denoising step. In the denoising term, $X^{k+1} - D_3^k$ is regarded as the “noisy” observed image, and V_3 is regarded as the “clean” estimated image. Thus, the denoising term becomes the optimization of the residual between $(X^{k+1} - D_3^k)$ and V_3 by using regularizer φ .

In [54], Venkatakrishnan et al. proposed to replace φ by using different off-the-shelf image denoisers in ADMM iterations. The new challenge of the assumption is whether the algorithm will converge. This critical problem has been studied and discussed in the literature [55]. For many image reconstruction problems this algorithm has been demonstrated with competitive performance.

In this thesis, the proposed GIBM3D denoising algorithm is utilized in each iteration of the ADMM algorithm. GIBM3D is used as the regularizer φ on the “noisy” image $(X^{k+1} - D_3^k)$ to generate the “clean” denoised image V_3 in each ADMM iteration. Hence, for GIBM3D regularizer the solution to V_3^{k+1} is given as follows.

$$V_3^{k+1} = \varphi(X^{k+1} - D_3^k) \quad (3.24)$$

Here GIBM3D algorithm replaces the regularizer φ . Afterwards, we return the value of V_3^{k+1} to update the Lagrange multipliers and perform the iterations until the criteria is satisfied. The overall ADMM algorithm with all its steps is given in Alg.1.

Algorithm 1: ADMM- GIBM3D pansharpening

Input: $Y_h, Y_p, R, B, E, M, \lambda_p, \mu$, guiding image;

- 1: Initialization: $D_1^0 = D_2^0 = D_3^0 = \text{Initial image}, V_1^0 = V_2^0 = V_3^0 = \text{Initial image};$
- 2: **for** $k := 0, 1, 2, 3, \dots K$, **do**
- 3: Compute X^{k+1} by applying (3.19);
- 4: Compute V_1^{k+1} by applying (3.20);
- 5: Compute V_2^{k+1} by applying (3.21);
- 6: Compute V_3^{k+1} by applying (3.24); the GIBM3D is used here.
- 7: Renew D_1^{k+1} by applying (3.16);
- 8: Renew D_2^{k+1} by applying (3.17);
- 9: Renew D_3^{k+1} by applying (3.18);
- 10: $k := k+1;$
- 11: **end for**
- 12: Obtain high spatial resolution MS/HS image: $\hat{Z} = EX^{K+1};$
- 13: **Output:** $\hat{Z}.$



4. SIMULATION

4.1 Performance measurement

The easiest approach to measure the quality of estimated image is by human eyes. However, due to the subjectivity of visual evaluation, the quality of an image may vary from one person to another. Therefore, it is critical to set up numerical measurement approaches for quality assessment.

Generally, the absence of reference image in satellite image processing techniques makes it hard to quantitatively measure the quality of estimated image.

To solve the problem of not existing original reference image, Wald *et al* [56] proposed to synthesize the MS/HS and PAN image from the given available MS/HS images used as a reference. Zhou *et al.* [57] proposed to assess the pansharpened image with observed images respectively to get the corresponding spectral and spatial distortion. Also, there are other approaches that use no reference, like Quality with No Reference (QNR) index [58].

4.1.1 Visual evaluation

The visual evaluation as shown in Table 4.1 can be implemented on the sharpness, contrast, texture and size of roads, cars and buildings of the pansharpened image according specific application.

Table 4.1: Visual evaluation for image quality assessment [59].

Grade	Absolute assessment	Relative assessment in a group
1	Excellent	The best level
2	Good	Better than average level
3	Fair	Average level
4	Poor	Lower than average level
5	Very Poor	The lowest

Visual evaluation is more dependent on the evaluator’s experience and also on viewing conditions. However, evaluation points can be also allocated to quantify the quality of the image qualitatively [59]. Then, a weighted mean on each item is calculated to obtain the final overall quality score.

4.1.2 Quantitative evaluation with reference

In [56], Wald *et al.* proposed a general paradigm (Figure 4.1) that is widely used for assessing the fused image quantitatively. They proposed to synthetically generate the observed image from the given available MS/HS image, which is utilized as a reference. Then, they pansharpen the observed images and assess the estimated results by comparing with reference. This assessment is based on the consistency and synthesis properties of a well-pansharpened image. These properties firstly require that the given MS/HS image ought to get generated as close as possible with proper degradation from synthetic pansharpened image. Secondly, this synthetic estimated image ought to be close to true high spatial quality MS/HS image.

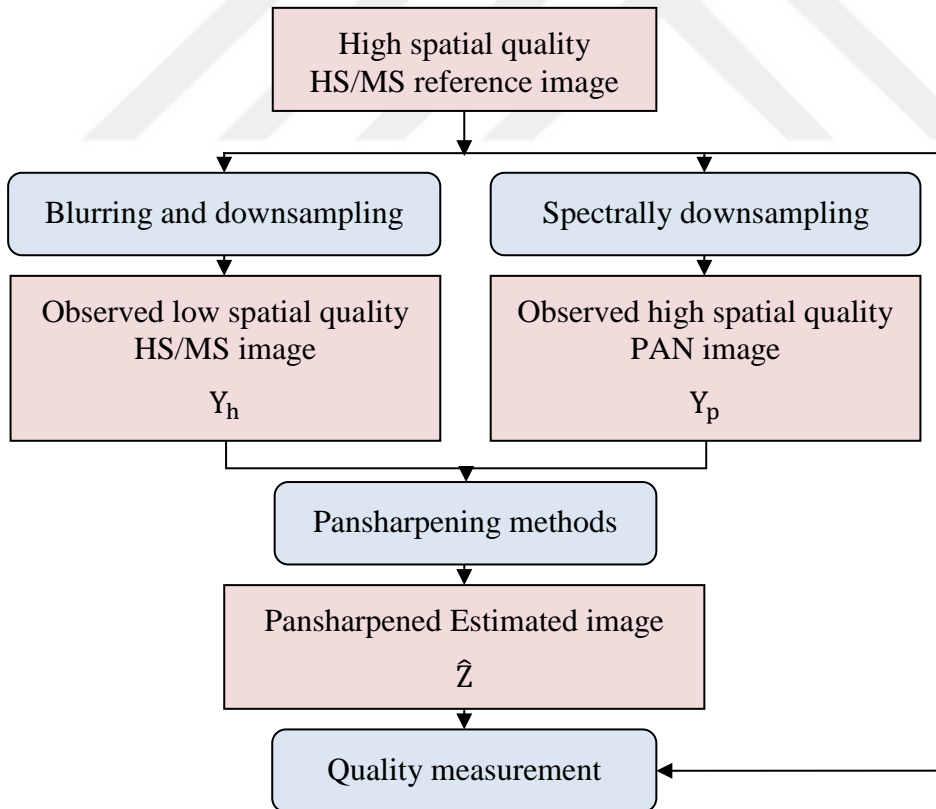


Figure 4.1: Flowchart for Wald’s protocol [12].

For the quantitative analysis of pansharpening performance, many quality measurement metrics have been proposed. In this thesis, five widely utilized quality evaluation metrics are presented for performance comparisons among pansharpening methods. Namely these are the root mean square error (RMSE), erreur relative globale adimensionnelle de synthèse (ERGAS: relative dimensionless global error), the spectral angular mapper (SAM), the peak signal-to-noise ratio (PSNR) and the cross correlation (CC). Let $\hat{X} \in \mathbb{R}^{L_h \times n_p}$ denote estimated image and $X \in \mathbb{R}^{L_h \times n_p}$ denote reference image both having L_h bands and n_p pixels in each band.

RMSE: It is used to evaluate ℓ_2 error between estimated image \hat{X} and reference X by computing the variation pixelwise.

$$\text{RMSE}(\hat{X}, X) = \frac{\|\hat{X} - X\|_F}{\sqrt{L_h * n_p}} \quad (4.1)$$

$\|X\|_F$ is the ℓ_2 norm (Euclidean distance) of X . The closer the estimated image \hat{X} is to reference X , the less ℓ_2 error there will be and the closer the value of RMSE is to 0. The ideal RMSE value is 0.

ERGAS [60] is utilized to evaluate final estimated image pertaining to normalized average error over each band. Increasing value of ERGAS may be attributed to the distortion of the estimated image. Lower value indicates more similar result to the reference image.

$$\text{ERGAS}(\hat{X}, X) = 100d \sqrt{\frac{1}{L_h} \sum_{k=1}^{L_h} \left(\frac{\text{RMSE}_k}{\text{mean}(X^k)} \right)^2} \quad (4.2)$$

Here, k represents the k th band. RMSE_k is the k th band $\text{RMSE}_k = \|\hat{X}^k - X^k\|_F / \sqrt{n_p}$, and d is defined as the spatial resolution ratio of observed images.

PSNR assesses the final estimated image in terms of maximum possible value to the noise in decibels (dB). For an 8-bit gray level image, the maximum possible value is, $\text{MAX}_I = 2^8 - 1 = 255$. The better pansharpened image generally produces higher PSNR. However, due to the sensitivity variation of human eye's response to the error, PSNR may not be proportional to visual quality.

$$\text{PSNR} = 20 \cdot \log_{10} \frac{\text{MAX}_I}{\text{RMSE}} \quad (4.3)$$

CC is used to assess the spatial quality and is defined as follows:

$$\text{CC}(\widehat{X}, X) = \frac{1}{L_h} \sum_{k=1}^{L_h} \text{CCS}(\widehat{X}^k, X^k) \quad (4.4)$$

Let A, B represent two single-band images with same size n_p . $\mu_A = \frac{1}{n_p} \sum_{j=1}^{n_p} A_j$ is mean value of A. CCS is defined as follows.

$$\text{CCS}(A, B) = \frac{\sum_{j=1}^{n_p} (A_j - \mu_A)(B_j - \mu_B)}{\sqrt{\sum_{j=1}^{n_p} (A_j - \mu_A)^2 \sum_{j=1}^{n_p} (B_j - \mu_B)^2}} \quad (4.5)$$

SAM is a significant metric to quantify the spectral distortion. Let $\mathbf{x}_{\{n\}} = [\mathbf{x}_{1, \{n\}}, \dots, \mathbf{x}_{L_h, \{n\}}]$ denote the n th pixel vector of the reference X which has L_h bands. Then the SAM for estimated image \widehat{X} and reference X is defined as given below.

$$\text{SAM}(\widehat{X}, X) = \frac{1}{n_p} \sum_{j=1}^{n_p} \arccos \left(\frac{\langle \widehat{\mathbf{x}}_{\{n\}}, \mathbf{x}_{\{n\}} \rangle}{\|\widehat{\mathbf{x}}_{\{n\}}\|_F \|\mathbf{x}_{\{n\}}\|_F} \right) \quad (4.6)$$

Here, $\langle \widehat{\mathbf{x}}_{\{n\}}, \mathbf{x}_{\{n\}} \rangle = \widehat{\mathbf{x}}_{\{n\}}^T \mathbf{x}_{\{n\}}$ is the inner product between $\widehat{\mathbf{x}}_{\{n\}}$ and $\mathbf{x}_{\{n\}}$. SAM measures the performance to preserve the spectrum, and its optimal value is zero which denotes the spectral shape of the estimated image completely matches that of the reference image without any spectral distortion.

4.1.3 Quantitative evaluation without reference

In [58], QNR protocol is proposed to evaluate the pansharpened image without any reference. QNR includes two basic indexes, D_λ which represents spectral distortion and D_s which represents spatial distortion. QNR is obtained with Quality Index (QI) which was proposed in [61].

For an image x as a reference and an image y to be compared, the corresponding QI is defined below.

$$Q(x, y) = \frac{4\sigma_{xy} \cdot \bar{x} \cdot \bar{y}}{(\sigma_x^2 + \sigma_y^2)(\bar{x}^2 + \bar{y}^2)} \quad (4.7)$$

Here, σ_{xy} represents covariance coefficient of image x and y . \bar{x} and \bar{y} represent average values of x and y . σ_x^2 represents variance of image x . σ_y^2 represents variance of image y .

For the spectral distortion index D_λ , it is obtained by calculating the diversity between the QI of fused image bands and the QI of given observed low-resolution MS/HS image bands. D_λ is defined as,

$$D_\lambda = \sqrt[p]{\frac{1}{L_h(L_h-1)} \sum_{l=1}^{L_h} \sum_{r=1, r \neq l}^{L_h} |Q(\widehat{G}_l, \widehat{G}_r) - Q(\widetilde{G}_l, \widetilde{G}_r)|^p} \quad (4.8)$$

where L_h denotes band number. $Q(\widehat{G}_l, \widehat{G}_r)$ is QI of two bands in fused image \widehat{G} . $Q(\widetilde{G}_l, \widetilde{G}_r)$ is the QI of two bands in given observed low spatial quality MS/HS image. p can be regarded as the used norm value, and it can take values such as $p=1$ or $p=2$.

For the spatial distortion index D_s , it is obtained by calculating the diversity of QI of final estimated image with observed PAN image to QI of observed MS/HS image with same scale PAN image.

$$D_s = \sqrt[q]{\frac{1}{L_h} \sum_{l=1}^{L_h} |Q(\widehat{G}_l, P) - Q(\widetilde{G}_l, \widetilde{P})|^q} \quad (4.9)$$

Here, L_h is total band number. \widehat{G}_l is estimated image. P represents observed PAN image. \widetilde{G}_l represents observed MS/HS image. \widetilde{P} represents the MS/HS-scale degraded observed PAN image. Q denotes the QI; q can be regarded as the norm value.

Although keeping D_λ and D_s separate is essential for the sake of comparison, a single index QNR [58] is proposed to trade off the D_λ and D_s values.

$$QNR = (1 - D_\lambda)^\alpha \cdot (1 - D_s)^\beta \quad (4.10)$$

α and β are used to balance the importance of the spectral and spatial quality respectively. Generally, α and β are set to one, indicating the same importance.

D_λ and D_s denote spectral distortion and spatial distortion respectively. In contrast, $(1-D_\lambda)$ and $(1-D_s)$ denote spectral quality and spatial quality respectively. For D_λ and D_s the expected ideal values are zeros and for QNR it is one which indicate there is no spectral and spatial distortions.

4.2 Datasets

Three Hyperspectral datasets and three multispectral datasets are used for simulations in this thesis [12]. Because of the unavailability of PAN images in the datasets, the PAN and HS images used in this thesis are generated from the given available datasets. They will be used as references in line with the Wald's protocol.

The detailed summaries of all datasets are listed in Table 4.2.

Table 4.2: Properties of the datasets.

Datasets	Dimensions		Ratio	Bands	Instruments
Moffett	PAN 95×185	HS 19×37	5	176	AVIRIS
KSC	PAN 150×150	HS 30×30	5	142	AVIRIS
DE2	PAN 500×500	MS 100×100	5	4	DEIMOS-2
IK	PAN 320×320	MS 64×64	5	4	IKONOS
WV2	PAN 320×320	MS 64×64	5	8	World View-2

(1) The Moffett field dataset: The size of this HS dataset is 395×185×176 (too noisy bands were removed). The spatial resolution is 20m covering a spectral range 0.4–2.5 μ m. This imageset is taken by Airborne Visible and Infrared Imaging Spectrometer (AVIRIS). For generated PAN image, its dimension is 95×185 and for generated HS image it is 19×37 with a downsampling ratio of five.

(2) The Kennedy Space Center (KSC) dataset: The size of this dataset is 512×614×142 (some low SNR noisy bands are removed from the original dataset). The spatial resolution is 18m covering a spectral range 0.4–2.5 μ m. This dataset is acquired by NASA AVIRIS. For generated PAN image, its dimension is 150×150 and for generated HS image it is 30×30 with a downsampling ratio of five.

(3) Multispectral datasets: The three MS datasets are acquired by DEIMOS-2, GeoEye1, World View2 and IKONOS respectively.

4.3 Implementation

The PAN and MS/HS images are synthesized from given MS/HS datasets respectively in accordance with Wald's protocol [56].

In terms of the general comparisons among different pansharpening methods, some well-known methods, which are utilized for both Multispectral and Hyperspectral pansharpening, are selected. These methods include PCA, GFPCA, GS, GSA from the CS group and HPF, SFIM from the MRA group. All these methods have been analyzed in detail in section 2.

For comparison with pansharpening methods from the model-based category, ADMM-BM3D and HySure methods are selected. In the experiments, the results of ADMM-BM3D methods vary greatly, with serious stripe noise especially in the case of hyperspectral pansharpening. To solve this problem, an initiation is assigned to the iteration parameters. The initiation used in this thesis for the convenience of comparison is generated from the HySure method with 100 iterations.

The guiding images used in ADMM-GIBM3D pansharpening are the same as the initial images used in the ADMM-BM3D methods for the convenience of comparison although the better guiding images produce the better results. There is no initiation used for ADMM-GIBM3D methods.

For the comparison of ADMM-GIBM3D, ADMM-BM3D and HySure methods, the iteration numbers are set to the same value of 100 iterations. Parameters λ_p and μ stay the same (with those in HySure method) for all the datasets with fixed values. Subspace E is removed in the multispectral pansharpening experiments due to less spectral bands.

The sigma used in ADMM-BM3D and ADMM-GIBM3D-thw is decreasing adaptively with the iteration process. The sigma used in ADMM-GIBM3D-wth is calculated from the diversity between the input and output of the Wiener filtering step.

4.4 Results and comparisons

In terms of BM3D, Eksioglu and Tanc [62] proposed for image reconstruction to use a single Hard-thresholding step instead of the full two steps, since the Wiener filtering step does not obviously enhance performance in spite of increasing computational complexity. The assumption is also validated successfully in all the experiments of the ADMM-BM3D method in this thesis. Therefore, for the ADMM- BM3D method only the results of the single Hard-thresholding step are used for comparison.

As to the ADMM-GIBM3D method, the three sub-models produce similar results in all the experiments by using the same λ_p and μ with a properly optimized sigma. The only difference is that ADMM-GIBM3D-w consumes the least time. For this reason, the results used for comparison are taken from the ADMM-GIBM3D-w method. The results of trying different multiple values for sigma in ADMM-GIBM3D-w method also demonstrate that sigma does not affect the Wiener filtering step except the consumed time. The bigger sigma results in higher computation time. Therefore, in ADMM-GIBM3D-w method, sigma value is set to zero.

4.4.1 Visual comparison

The pansharpening results of all methods for all datasets with the reference (REF) original MS/HS images have been visualized for visual comparison by combining the second to the fourth bands from Figure 4.2 (a) to Figure 4.6 (a). Figure 4.2 (b) to Figure 4.6 (b) are the 10 times residue of pansharpening results with the REF image for the sake of showing the differences between REF image and various pansharpening results. That is $\text{Residue} = 10 * (\text{REF} - \text{result-image})$.

For all the datasets, it is apparent that GFPCA produces most blurs compared to other methods. In GFPCA a lot of details are missing. PCA performs better than GFPCA in all datasets and even better than HPF and SFIM in edge preserving for DE2, IK, dataset. For WV2 and two Hyperspectral datasets, HPF and SFIIM preserves more clear edge details than PCA. For all datasets, GSA appears better edge preserving performance than GS method. In terms of the residue images, PCA, GFPCA and GS results are showing significant difference with the REF image. For spectral information

preservation, in IK and WV2 dataset, PCA, GFPCA and GS perform poorly displaying serious color distortion.

The three model based methods HySure, ADMM-BM3D and ADMM-GIBM3D give indistinguishably good results with GSA method from Figure 4.2 (a) to Figure 4.6 (a). Regarding the residue image from Figure 4.2 (b) to Figure 4.6 (b), the three model based methods together with GSA also keep the least residue with the REF image. Furthermore, proposed ADMM-GIBM3D keeps less residue than HySure and ADMM-BM3D method. This indicates that proposed ADMM-GIBM3D method can produce the closest result to REF. Generally, MRA category methods keep spectral information better than CS category. Model based method appears better edge and spectral preservation performance than CS and MRA category.

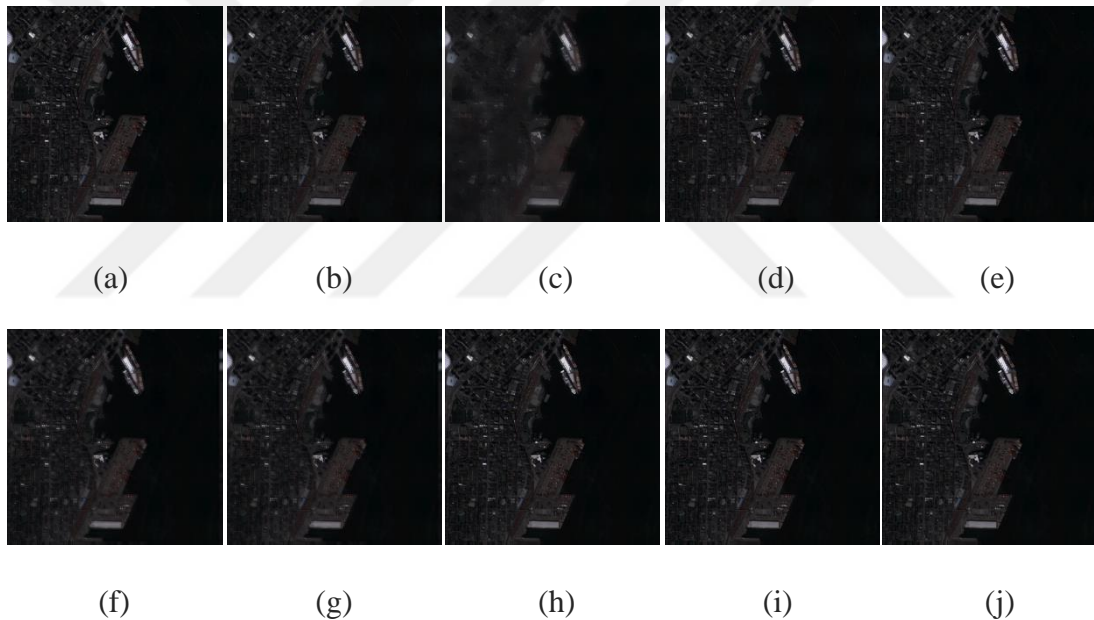


Figure 4.2 (a): Pansharpened images for DE2 dataset: (a) REF; (b) PCA; (c) GFPCA; (d) GS; (e) GSA; (f) HPF; (g) SFIM; (h) HySure; (i) ADMM-BM3D; (j) ADMM-GIBM3D;

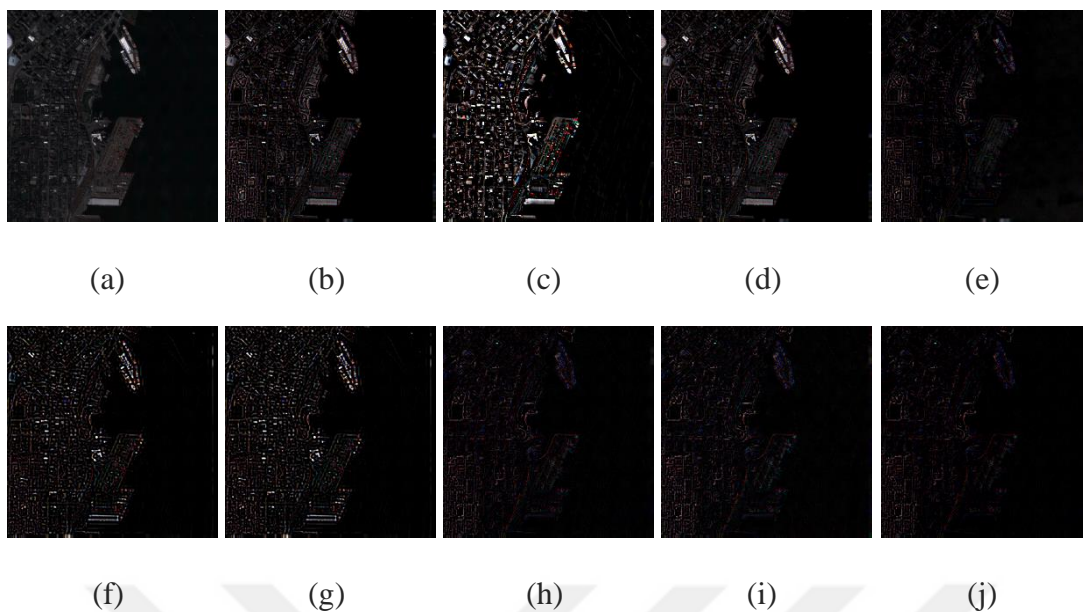


Figure 4.2 (b): Pansharpened image residue with REF for DE2 dataset: (a) REF; (b) PCA; (c) GFPCA; (d) GS; (e) GSA; (f) HPF; (g) SFIM; (h) HySure; (i) ADMM-BM3D; (j) ADMM-GIBM3D;

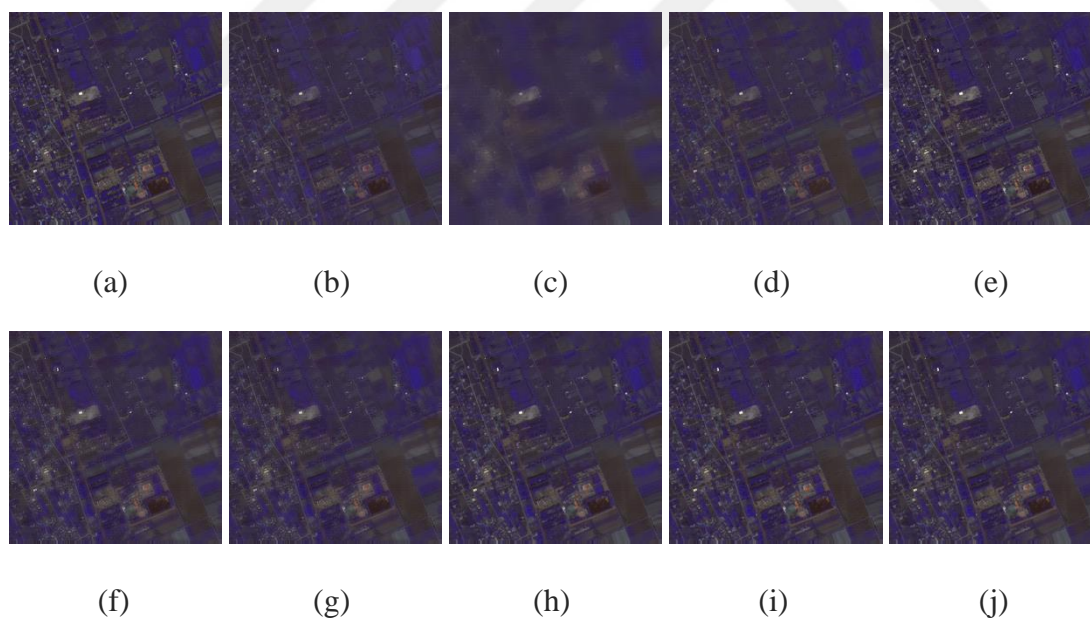


Figure 4.3 (a): Pansharpened images for IK dataset : (a) REF; (b) PCA; (c) GFPCA; (d) GS; (e) GSA; (f) HPF; (g) SFIM; (h) HySure; (i) ADMM-BM3D; (j) ADMM-GIBM3D;

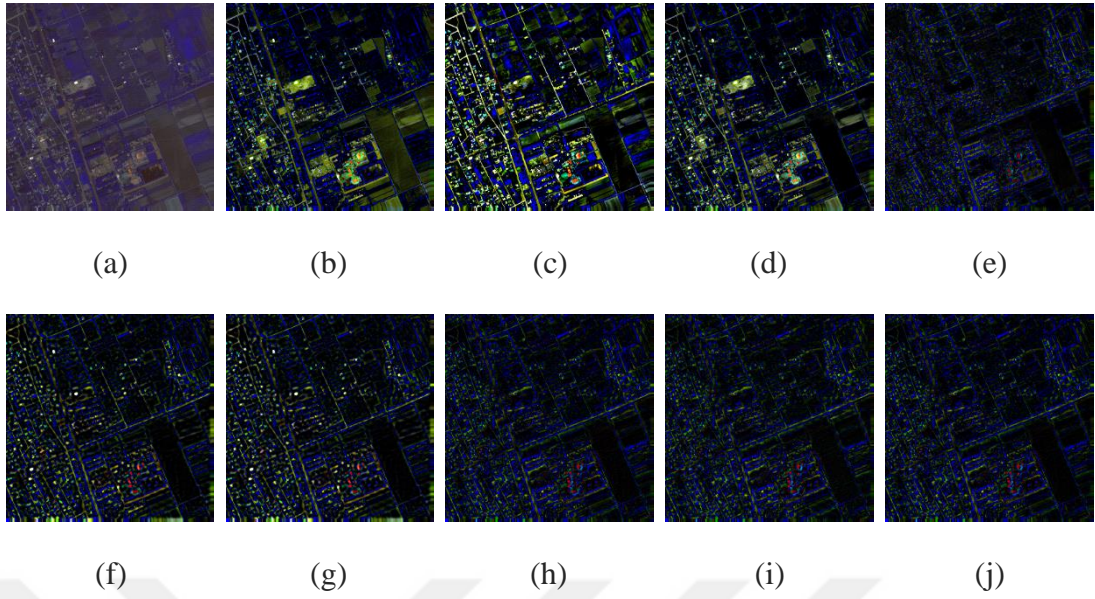


Figure 4.3 (b): Pansharpened image residue with REF for IK dataset: (a) REF; (b) PCA; (c) GFPCA; (d) GS; (e) GSA; (f) HPF; (g) SFIM; (h) HySure; (i) ADMM-BM3D; (j) ADMM-GIBM3D;

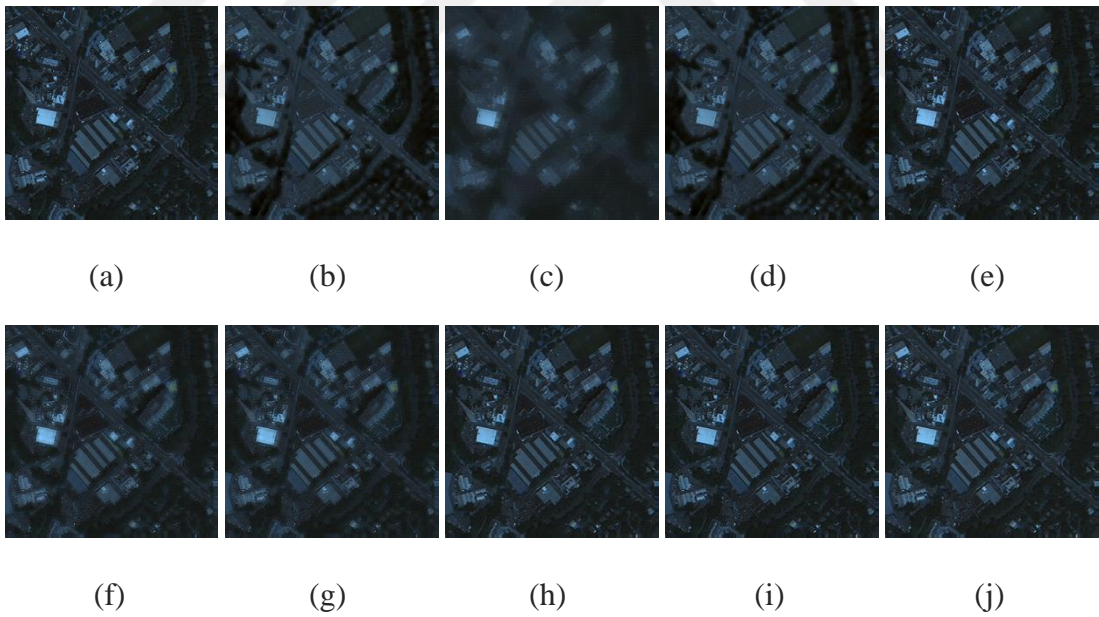


Figure 4.4 (a): Pansharpened images for WV2 dataset: (a) REF; (b) PCA; (c) GFPCA; (d) GS; (e) GSA; (f) HPF; (g) SFIM; (h) HySure; (i) ADMM-BM3D; (j) ADMM-GIBM3D;

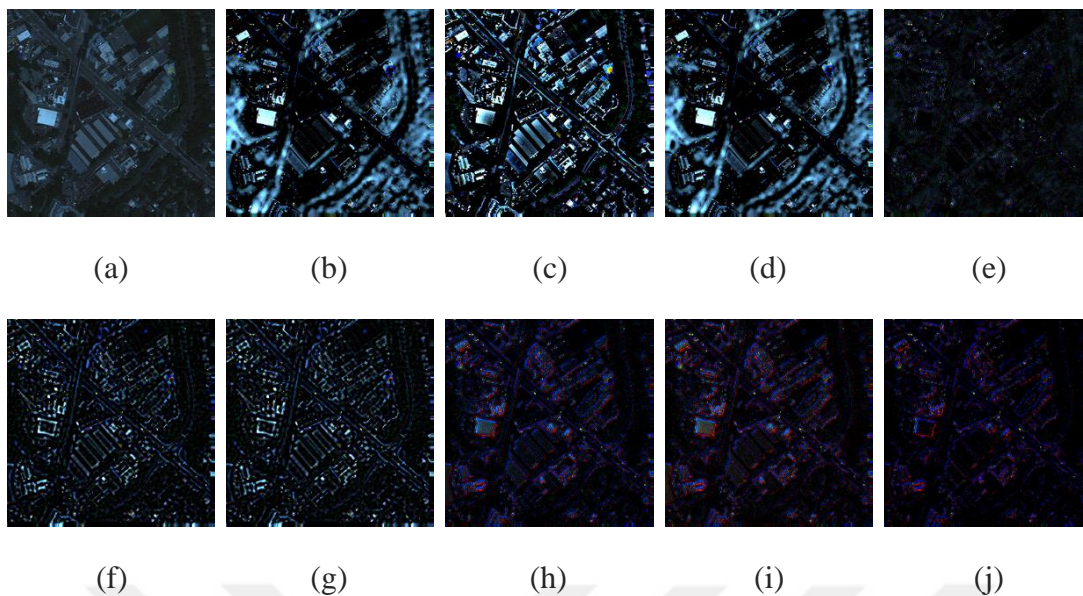


Figure 4.4 (b): Pansharpened image residue with REF for WV2 dataset: (a) REF; (b) PCA; (c) GFPCA; (d) GS; (e) GSA; (f) HPF; (g) SFIM; (h) HySure; (i) ADMM-BM3D; (j) ADMM-GIBM3D;

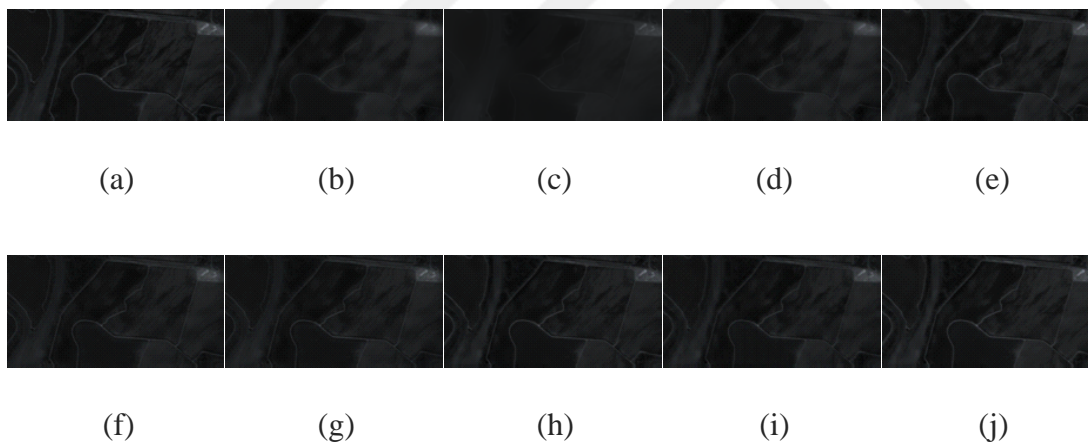


Figure 4.5 (a): Pansharpened images for Moffett dataset: (a) REF; (b) PCA; (c) GFPCA; (d) GS; (e) GSA; (f) HPF; (g) SFIM; (h) HySure; (i) ADMM-BM3D; (j) ADMM-GIBM3D;

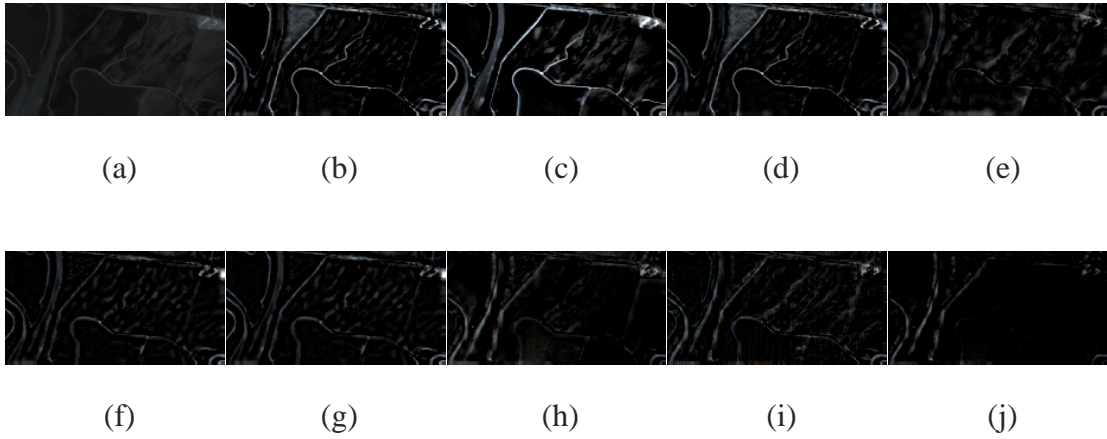


Figure 4.5 (b): Pansharpened image residue with REF for Moffett dataset: (a) REF; (b) PCA; (c) GFPCA; (d) GS; (e) GSA; (f) HPF; (g) SFIM; (h) HySure; (i) ADMM-BM3D; (j) ADMM-GIBM3D;

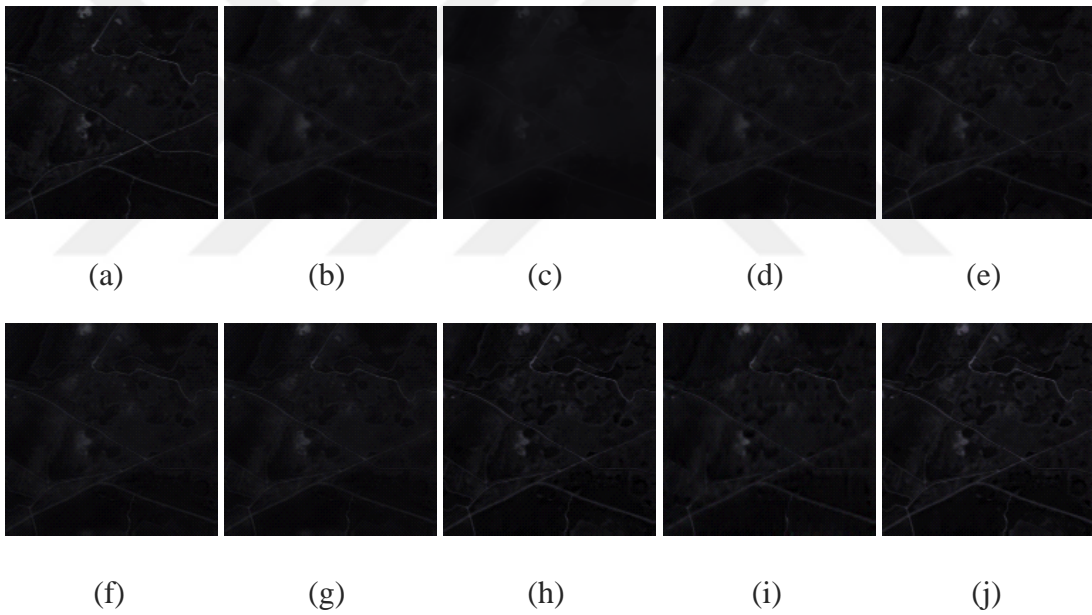


Figure 4.6 (a): Pansharpened image for KSC dataset: (a) REF; (b) PCA; (c) GFPCA; (d) GS; (e) GSA; (f) HPF; (g) SFIM; (h) HySure; (i) ADMM-BM3D; (j) ADMM-GIBM3D;

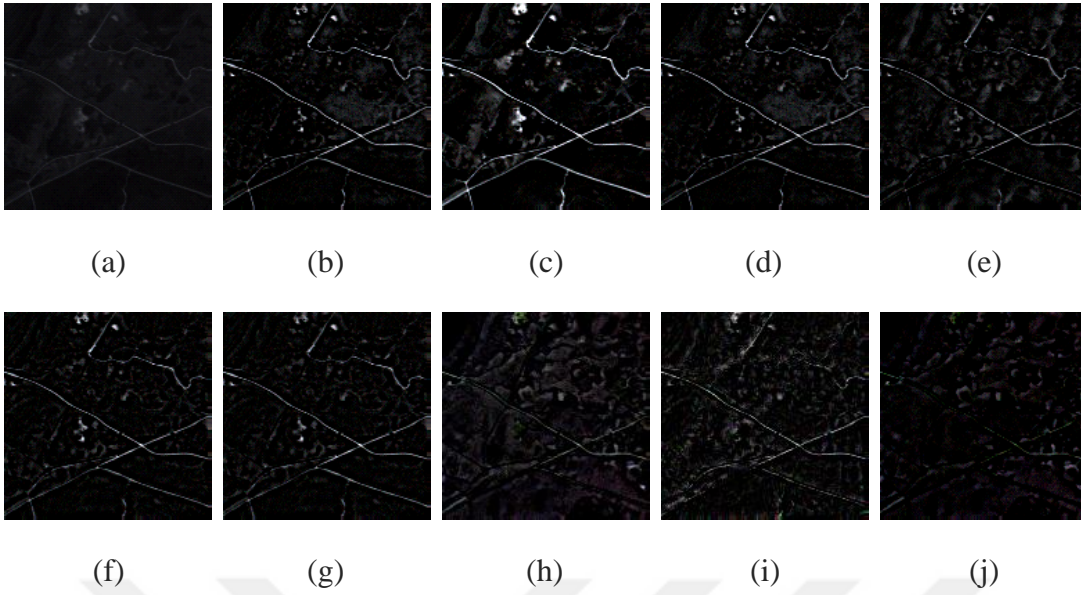


Figure 4.6 (b): Pansharpened image residue with REF for KSC dataset: (a) REF; (b) PCA; (c) GFPCA; (d) GS; (e) GSA; (f) HPF; (g) SFIM; (h) HySure; (i) ADMM-BM3D; (j) ADMM-GIBM3D;

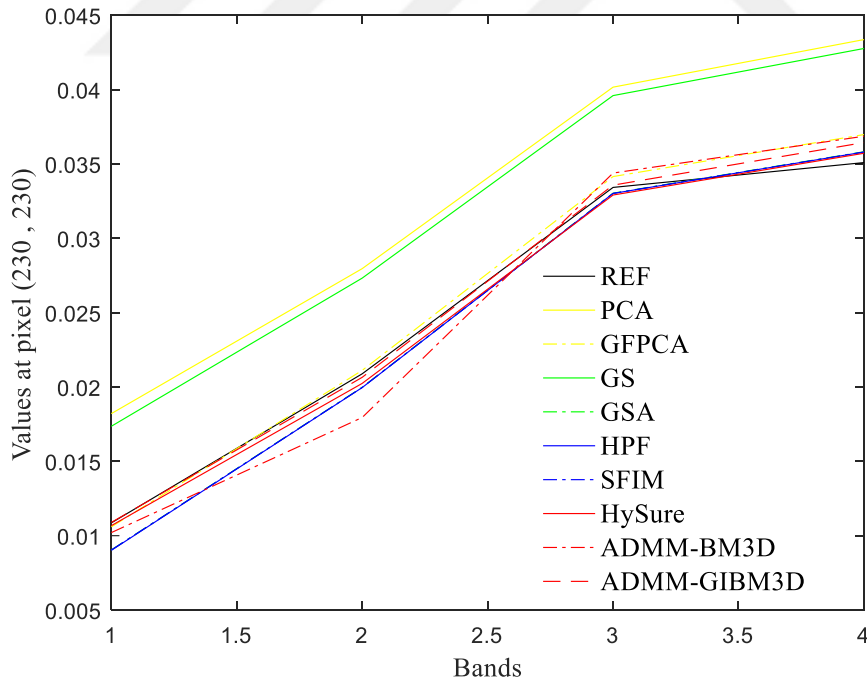


Figure 4.7: Spectrum for DE2 dataset.

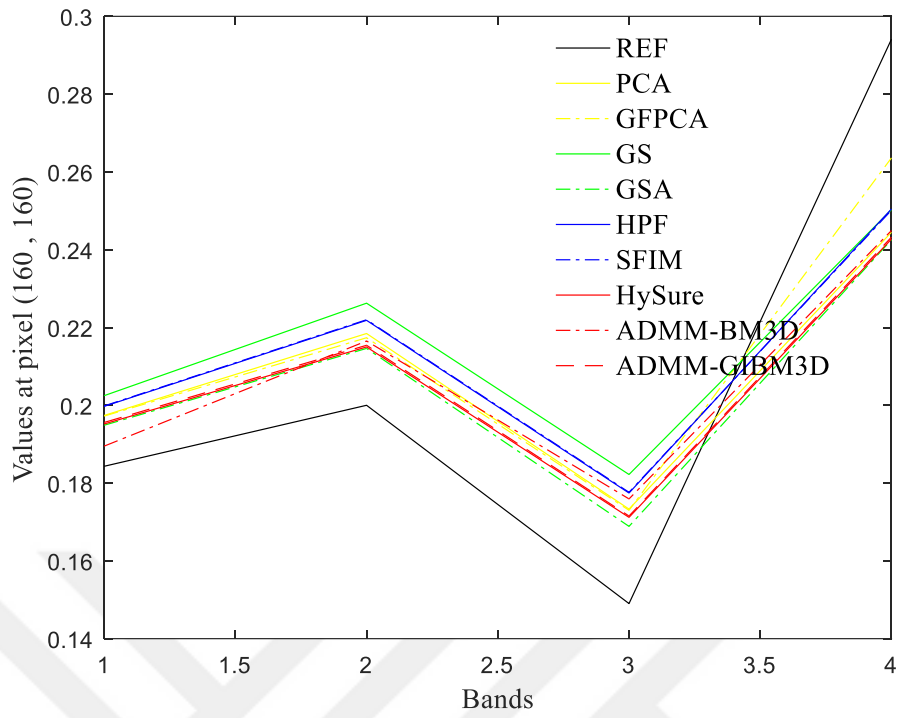


Figure 4.8: Spectrum for IK dataset.

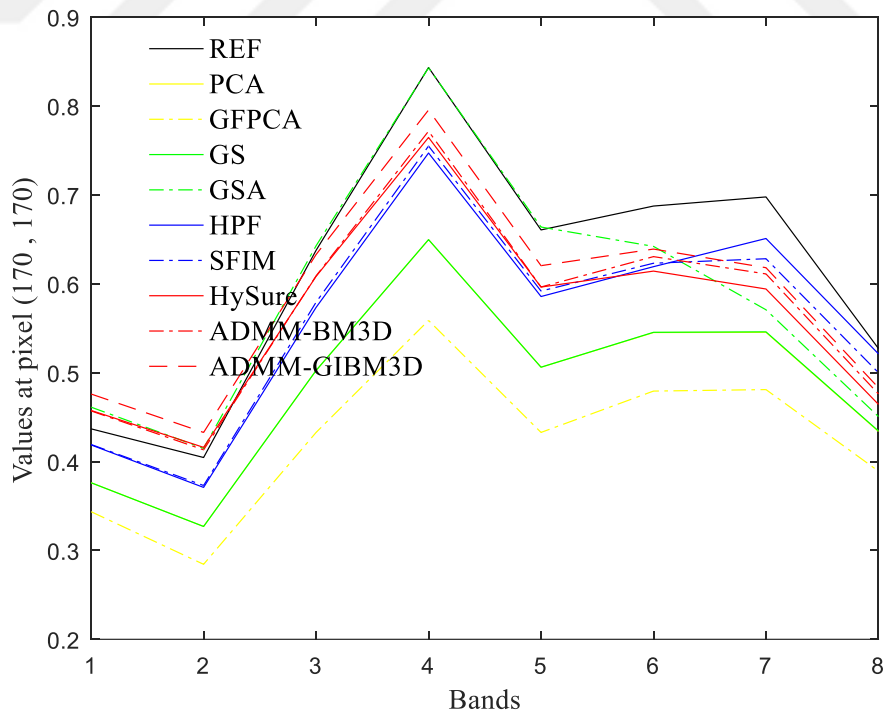


Figure 4.9: Spectrum for WV2 dataset.

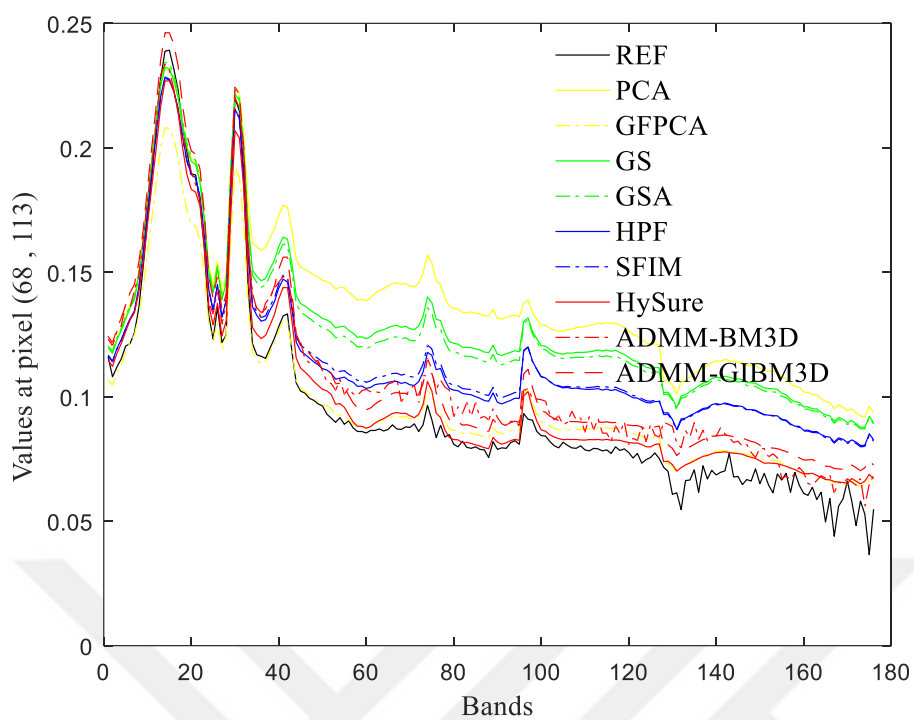


Figure 4.10: Spectrum for Moffett dataset.

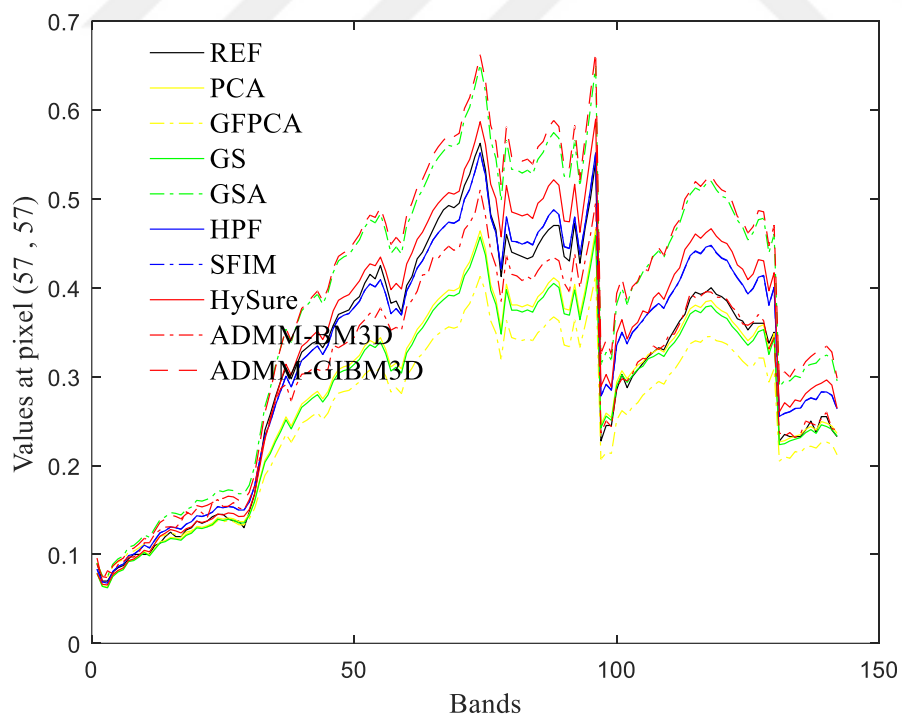


Figure 4.11: Spectrum for KSC dataset.

From Figure 4.7 to Figure 4.11, the spectrum of some specific pixels is compared. Generally, CS family methods (yellow and green lines) differ much more than the MRA family methods (blue lines) with the reference image (black lines). And model based methods (red lines) also perform as well as MRA methods.

4.4.2 Quantitative comparisons with reference

The quantitative results with reference are calculated according to Wald’s protocol. Table 4.3 to Table 4.7 show the quantitative comparisons for all datasets. For better inter-categories comparison, the best result among all the realized methods is marked with bold. For better comparison of the three model-based methods, the best result for these three are marked with a shaded (gray) background. GSA, HPF and SFIM having 9, 11 and 6 bolds respectively outperform other methods. In model based methods, ADMM-GIBM3D give better results except rmse and time. This shows the competitiveness of the proposed ADMM-GIBM3D method amongst the model-based family. For different guiding images generated from different pansharpening results, the proposed ADMM-GIBM3D method also shows competitive performance compared to the original method which generates the corresponding guiding image.

Table 4.3: Quantitative results with reference for DE2 dataset.

DE2 dataset	CC	SAM	RMSE	ERGAS	PSNR	time
Ideal value	1	0	0	0	higher	lower
PCA	0,9894	5,8605	0,0156	3,6768	34,6477	0,3118
GFPCA	0,9287	5,1109	0,0319	7,5884	28,1324	1,1729
GS	0,9898	5,6364	0,0155	3,6544	34,6195	0,3339
GSA	0,9888	4,1851	0,0132	3,0645	36,9172	0,3989
HPF	0,9810	3,9598	0,0167	3,9688	34,7251	0,2895
SFIM	0,9824	3,7913	0,0162	3,8698	35,1904	0,3201
HySure	0,9889	3,9885	0,0132	3,0755	36,8757	83,4138
ADMM-BM3D	0,9885	5,0098	0,0134	3,1162	36,8133	203,8823
ADMM-GIBM3D	0,9889	3,9883	0,0134	3,0517	36,9512	153,5285

Table 4.4: Quantitative results with reference for IK dataset.

IK dataset	CC	SAM	RMSE	ERGAS	PSNR	time
Ideal value	1	0	0	0	higher	lower
PCA	0,8963	4,0410	0,0280	2,3392	29,9430	0,1324
GFPCA	0,7481	4,6081	0,0380	3,3043	23,2260	0,1109
GS	0,9306	3,5063	0,0251	2,1057	30,0906	0,1099
GSA	0,9413	3,4731	0,0196	1,5839	35,9752	0,1256
HPF	0,9257	3,4105	0,0218	1,8425	32,9526	0,0811
SFIM	0,9270	3,3696	0,0218	1,8349	32,4023	0,0801
HySure	0,9364	3,5960	0,0201	1,6381	34,2653	25,6522
ADMM-BM3D	0,9331	3,7145	0,0203	1,6653	34,0363	136,1183
ADMM-GIBM3D	0,9364	3,5960	0,0201	1,6350	34,2840	91,0323

Table 4.5: Quantitative results with reference for WV2 dataset.

WV2 dataset	CC	SAM	RMSE	ERGAS	PSNR	time
Ideal value	1	0	0	0	higher	lower
PCA	0,8722	8,6261	0,0609	5,7297	24,2597	0,4633
GFPCA	0,8023	10,3976	0,0732	6,8833	22,2338	1,4245
GS	0,8749	8,5673	0,0604	5,6762	24,3979	0,7539
GSA	0,9297	8,2892	0,0484	4,0397	29,3080	0,4412
HPF	0,9270	7,5992	0,0477	4,2001	28,1834	0,2216
SFIM	0,9259	7,5537	0,0483	4,2461	26,3295	0,2548
HySure	0,9086	8,6340	0,0533	4,6670	25,8068	46,6929
ADMM-BM3D	0,9055	8,8545	0,0535	4,6167	25,8205	134,5606
ADMM-GIBM3D	0,9086	8,6334	0,0535	4,5222	26,1193	107,7844

Table 4.6: Quantitative results with reference for Moffett dataset.

Moffett dataset	CC	SAM	RMSE	ERGAS	PSNR	time
Ideal value	1	0	0	0	higher	lower
PCA	0,8038	16,5241	0,0696	12,0569	26,4846	1,8505
GFPCA	0,8232	13,7447	0,0656	12,2503	20,8100	3,6588
GS	0,8430	14,0699	0,0622	11,0238	26,7791	1,6488
GSA	0,9318	11,1127	0,0395	7,5600	29,2328	1,3620
HPF	0,9453	8,9908	0,0359	7,0792	30,7413	0,8454
SFIM	0,9118	11,3541	0,0468	8,8366	26,6038	1,0496
HySure	0,9307	9,9191	0,0413	7,7554	27,3271	17,4636
ADMM-BM3D	0,8965	10,5534	0,0488	9,3227	24,9682	820,6248
ADMM-GIBM3D	0,9310	9,8179	0,0424	7,2082	27,8199	522,5637

Table 4.7: Quantitative results with reference for KSC dataset.

KSC dataset	CC	SAM	RMSE	ERGAS	PSNR	time
Ideal value	1	0	0	0	higher	lower
PCA	0,8861	14,9901	0,0845	8,5738	27,0387	1,0487
GFPCA	0,8189	16,6642	0,1037	10,5030	19,2987	1,2294
GS	0,8913	15,0570	0,0832	8,4865	26,9780	1,1678
GSA	0,9072	19,5412	0,0756	7,8060	28,4345	0,8932
HPF	0,9188	14,3187	0,0682	7,2877	27,6012	0,6472
SFIM	0,9189	13,3505	0,0683	7,4157	23,3167	0,6627
HySure	0,9170	15,0357	0,0697	7,4223	25,9765	16,3478
ADMM-BM3D	0,9011	18,0114	0,0772	8,0010	24,9644	637,0878
ADMM-GIBM3D	0,9175	14,5590	0,0759	7,0825	26,2767	519,9057

4.4.3 QNR comparisons

The QNR and Scc results are shown from Table 4.8 to Table 4.12. QNR results show inconsistency with visual evaluation and quality metrics with reference. The most blurred results by GFPCA method here have the best QNR performance. Therefore, QNR is not regarded as the main quality measurement in this thesis.

Scc is the spatial cross correlation between PAN and result image. Scc better fits visual evaluation and quality metrics with reference than QNR metrics.

Table 4.8: Quantitative results without reference for DE2 dataset.

DE2 dataset	D_λ	D_s	QNR	Scc
Expected ideal value	0	0	1	1
PCA	0,1417	0,5777	0,3624	0,9855
GFPCA	0,1039	0,0239	0,8747	0,8556
GS	0,1397	0,5805	0,3609	0,9858
GSA	0,0920	0,5884	0,3738	0,9877
HPF	0,1086	0,4763	0,4669	0,9511
SFIM	0,0945	0,4352	0,5114	0,9420
HySure	0,1082	0,3087	0,6164	0,9838
ADMM-BM3D	0,1885	0,4538	0,4432	0,9768
ADMM-GIBM3D	0,1083	0,3135	0,6122	0,9838

Table 4.9: Quantitative results without reference for IK dataset.

IK dataset	D_λ	D_s	QNR	Scc
Expected ideal value	0	0	1	1
PCA	0,1149	0,5407	0,4066	0,8932
GFPCA	0,1451	0,0859	0,7815	0,7055
GS	0,1895	0,5987	0,3253	0,9325
GSA	0,2939	0,7445	0,1804	0,9643
HPF	0,2636	0,6115	0,2861	0,9354
SFIM	0,2635	0,6085	0,2883	0,9342
HySure	0,3022	0,7159	0,1983	0,9689
ADMM-BM3D	0,1964	0,6790	0,2579	0,9590
ADMM-GIBM3D	0,3022	0,7162	0,1980	0,9689

Table 4.10: Quantitative results without reference for WV2 dataset.

WV2 dataset	D_λ	D_s	QNR	Scc
Expected ideal value	0	0	1	1
PCA	0,1099	0,5395	0,4099	0,9070
GFPCA	0,0775	0,1168	0,8147	0,6885
GS	0,1090	0,5403	0,4096	0,9063
GSA	0,1202	0,5577	0,3891	0,8139
HPF	0,1797	0,5787	0,3456	0,8857
SFIM	0,1839	0,5558	0,3625	0,8747
HySure	0,1135	0,5293	0,4173	0,7663
ADMM-BM3D	0,0920	0,5262	0,4302	0,7483
ADMM-GIBM3D	0,1135	0,5344	0,4128	0,7663

Table 4.11: Quantitative results without reference for Moffett dataset.

Moffett dataset	D_λ	D_s	QNR	Scc
Expected ideal value	0	0	1	1
PCA	0,0890	0,3949	0,5512	0,8812
GFPCA	0,0290	0,1457	0,8295	0,8424
GS	0,0676	0,4284	0,5330	0,8935
GSA	0,0551	0,3511	0,6131	0,8889
HPF	0,0536	0,3624	0,6034	0,8716
SFIM	0,0711	0,3467	0,6069	0,7990
HySure	0,0501	0,3976	0,5722	0,8744
ADMM-BM3D	0,0707	0,2316	0,7140	0,7830
ADMM-GIBM3D	0,0503	0,4084	0,5619	0,8747

Table 4.12: Quantitative results without reference for KSC dataset.

KSC dataset	D_λ	D_s	QNR	Scc
Expected ideal value	0	0	1	1
PCA	0,0339	0,3794	0,5995	0,8906
GFPCA	0,0539	0,2611	0,6990	0,8047
GS	0,0342	0,3864	0,5926	0,8921
GSA	0,0380	0,3306	0,6440	0,8782
HPF	0,0479	0,3431	0,6254	0,8686
SFIM	0,0529	0,3361	0,6288	0,8566
HySure	0,0538	0,4112	0,5571	0,8717
ADMM-BM3D	0,0253	0,3367	0,6465	0,8252
ADMM-GIBM3D	0,0579	0,3923	0,5725	0,8728



5. CONCLUSIONS AND FUTURE WORK

5.1 Conclusions

Pansharpening is a significant technique utilized in remote sensing applications of image processing. The performance of pansharpening technique controls the quality of the final estimated image. In order to generate higher quality pansharpened images, many various pansharpening methods have been proposed. This thesis analyzed and compared different pansharpening methods and then proposed a new sparsity based pansharpening method.

This thesis analyzed some existing important pansharpening methods and compared the advantages and disadvantages, similarities and differences of various pansharpening methods. With these analysis and comparisons, this thesis classified pansharpening methods into CS category, MRA category and model based category methods. CS category pansharpening methods produce better spatial quality for MS images. MRA category methods produce better spectral quality for MS images. In terms of HS pansharpening, MRA category generally performs better than CS category. Model based methods perform well for both MS and HS pansharpening. However, model based methods consume much more time in comparison with CS and MRA category methods. Based on these previous works, this thesis proposed a novel pansharpening method using the newly proposed Guiding Image BM3D image denoising algorithm.

BM3D is an effective and powerful image denoising algorithm, which can be used as a prior in iterative pansharpening methods. Thanks to the need of a basic estimate image in the Wiener filtering step of the BM3D algorithm, some external guiding image can be added to enhance the performance of BM3D algorithm.

In this thesis, the GIBM3D denoising algorithm is proposed to enhance the performance of BM3D denoising algorithm when utilized in iterative pansharpening

techniques. The GIBM3D algorithm is coupled into each iteration of an iterative ADMM based solution for pansharpening. The introduction of the guiding image approach helps to improve the grouping and calculating the Wiener shrinkage coefficients in the Wiener filtering step of the BM3D algorithm when used for pansharpening. The better is the guiding image, the better are the pansharpening results produced by the introduced ADMM-GIBM3D algorithm

Three MS and two HS datasets are tested to demonstrate the performance of the proposed ADMM-GIBM3D pansharpening method. Experimental results have illustrate that the three proposed GIBM3D sub-models have the similar results except the required computational time for the case of same simulation parameters. The ADMM-GIBM3D-w sub-model has the least computational time requirement among the three introduced sub-models. Compared to the HySure method and the ADMM-BM3D method of the same category, the proposed ADMM-GIBM3D appears to have competitive performance.

5.2 Future work

In the thesis, the proposed GIBM3D is applied to ADMM iteration based multispectral and hyperspectral pansharpening techniques. In the future work, the three GIBM3D sub-model can be utilized in iterative algorithms, which solve different imaging inverse problems such as denoising, deblurring, superresolution and other possible applications.

REFERENCES

- [1] **S. Liang, X. Li, and J. Wang, Eds.**, 2012, Chapter 1 - A Systematic View of Remote Sensing, in *Advanced Remote Sensing*, Boston: Academic Press, pp. 1–31.
- [2] **H. Ghassemian**, 2016, A review of remote sensing image fusion methods, *Information Fusion*, vol. 32, pp. 75–89.
- [3] **X. Meng, H. Shen, H. Li, et al.**, 2019, Review of the pansharpening methods for remote sensing images based on the idea of meta-analysis: Practical discussion and challenges, *Information Fusion*, vol. 46, pp. 102–113.
- [4] **D. Picone, M. Dalla Mura, and L. Condat**, 2018, Pansharpening of images acquired with color filter arrays, in *SPIE Photonics Europe*, Strasbourg, France.
- [5] **F. Laporterie-Déjean, H. de Boissezon, G. Flouzat, and M.-J. Lefèvre-Fonollosa**, 2005, Thematic and statistical evaluations of five panchromatic/multispectral fusion methods on simulated PLEIADES-HR images, *Information Fusion*, vol. 6, no. 3, pp. 193–212.
- [6] **A. Mohammadzadeh, A. Tavakoli, and M. J. Valadan Zoej**, 2006, Road extraction based on fuzzy logic and mathematical morphology from pansharpened ikonos images, *The Photogrammetric Record*, vol. 21, no. 113, pp. 44–60.
- [7] **G. A. Licciardi, A. Villa, M. M. Khan, and J. Chanussot**, 2012, Image fusion and spectral unmixing of hyperspectral images for spatial improvement of classification maps, in *2012 IEEE International Geoscience and Remote Sensing Symposium*, pp. 7290–7293.
- [8] **C. Souza, L. Firestone, L. M. Silva, and D. Roberts**, 2003, Mapping forest degradation in the Eastern Amazon from SPOT 4 through spectral mixture models, *Remote Sensing of Environment*, vol. 87, no. 4, pp. 494–506.
- [9] **S. Baronti, B. Aiazzi, M. Selva, et al.**, 2011, A Theoretical Analysis of the Effects of Aliasing and Misregistration on Pansharpened Imagery, *IEEE Journal of Selected Topics in Signal Processing*, vol. 5, no. 3, pp. 446–453.
- [10] **G. Vivone, R. Restaino, G. Licciardi, et al.**, 2014, MultiResolution Analysis and Component Substitution techniques for hyperspectral Pansharpening, in *2014 IEEE Geoscience and Remote Sensing Symposium*, pp. 2649–2652.
- [11] **S. Li and B. Yang**, 2011, A New Pan-Sharpener Method Using a Compressed Sensing Technique, *IEEE Transactions on Geoscience and Remote Sensing*, vol. 49, no. 2, pp. 738–746.

- [12] **L. Loncan, L. B. de Almeida, J. M. Bioucas-Dias, et al.**, 2015, Hyperspectral Pansharpening: A Review, *IEEE Geoscience and Remote Sensing Magazine*, vol. 3, no. 3, pp. 27–46.
- [13] **H. Shen, X. Meng, and L. Zhang**, 2016, An Integrated Framework for the Spatio–Temporal–Spectral Fusion of Remote Sensing Images, *IEEE Transactions on Geoscience and Remote Sensing*, vol. 54, no. 12, pp. 7135–7148.
- [14] **J. Qu, Y. Li, and W. Dong**, 2018, Guided filter and principal component analysis hybrid method for hyperspectral pansharpening, *JARS*, vol. 12, no. 1, p. 015003.
- [15] **Q. Wei, N. Dobigeon, and J. Tourneret**, 2015, Bayesian Fusion of Multi-Band Images, *IEEE Journal of Selected Topics in Signal Processing*, vol. 9, no. 6, pp. 1117–1127.
- [16] **S. Li, H. Yin, and L. Fang**, 2013, Remote Sensing Image Fusion via Sparse Representations Over Learned Dictionaries, *IEEE Transactions on Geoscience and Remote Sensing*, vol. 51, no. 9, pp. 4779–4789.
- [17] **C. Jiang, H. Zhang, H. Shen, and L. Zhang**, 2012, A Practical Compressed Sensing-Based Pan-Sharpener Method, *IEEE Geoscience and Remote Sensing Letters*, vol. 9, no. 4, pp. 629–633.
- [18] **J. Duran, A. Buades, B. Coll, and C. Sbert**, 2014, A Nonlocal Variational Model for Pansharpening Image Fusion, *SIAM Journal on Imaging Sciences*, vol. 7, no. 2, pp. 761–796.
- [19] **M. Simões, J. Bioucas - Dias, L. B. Almeida, and J. Chanussot**, 2015, A Convex Formulation for Hyperspectral Image Superresolution via Subspace-Based Regularization, *IEEE Transactions on Geoscience and Remote Sensing*, vol. 53, no. 6, pp. 3373–3388.
- [20] **M. Simões, J. Bioucas-Dias, L. B. Almeida, and J. Chanussot**, 2014, Hyperspectral image superresolution: An edge-preserving convex formulation, in *2014 IEEE International Conference on Image Processing (ICIP)*, pp. 4166–4170.
- [21] **G. Scarpa, S. Vitale, and D. Cozzolino**, 2018, Target-Adaptive CNN-Based Pansharpening, *IEEE Transactions on Geoscience and Remote Sensing*, vol. 56, no. 9, pp. 5443–5457.
- [22] **X. Liu, Y. Wang, and Q. Liu**, 2018, PSGAN: A Generative Adversarial Network for Remote Sensing Image Pan-Sharpener, *arXiv:1805.03371 [cs]*.
- [23] **G. Masi, D. Cozzolino, L. Verdoliva, and G. Scarpa**, 2016, Pansharpening by Convolutional Neural Networks, *Remote Sensing*, vol. 8, no. 7, p. 594.
- [24] **Y. Wei, Q. Yuan, H. Shen, and L. Zhang**, 2017, Boosting the accuracy of multi-spectral image pan-sharpening by learning a deep residual network, *IEEE Geoscience and Remote Sensing Letters*, vol. 14, no. 10, pp. 1795–1799.
- [25] **P. S. Chavez and Andrew Yaw Kwarteng**, 1989, Extracting Spectral Contrast in Landsat Thematic Mapper Image Data Using Selective Principal Component

Analysis, *PHOTOGRAMMETRIC ENGINEERING AND REMOTE SENSING*, vol. 55, no. 3, pp. 339–348.

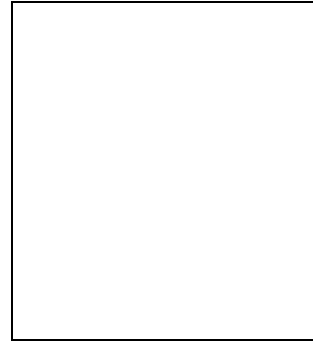
- [26] **W. Liao, X. Huang, F. V. Coillie, et al.**, 2015, Processing of Multiresolution Thermal Hyperspectral and Digital Color Data: Outcome of the 2014 IEEE GRSS Data Fusion Contest, *IEEE Journal of Selected Topics in Applied Earth Observations and Remote Sensing*, vol. 8, no. 6, pp. 2984–2996.
- [27] **C. A. Laben and B. V. Brower**, Process for enhancing the spatial resolution of multispectral imagery using pan-sharpening, US6011875A, 2000.
- [28] **B. Aiazzi, S. Baronti, and M. Selva**, 2007, Improving Component Substitution Pansharpening Through Multivariate Regression of MS+Pan Data, *IEEE Transactions on Geoscience and Remote Sensing*, vol. 45, no. 10, pp. 3230–3239.
- [29] **J. G. Liu**, 2000, Smoothing Filter-based Intensity Modulation: A spectral preserve image fusion technique for improving spatial details, *International Journal of Remote Sensing*, vol. 21, no. 18, pp. 3461–3472.
- [30] **P. S. Chavez, Stuart C. Sides, and Jeffrey A. Anderson**, 1991, Comparison of Three Different Methods to Merge Multiresolution and Multispectral Data:Landsat TM and SPOT Panchromatic, *PHOTOGRAMMETRIC ENGINEERING*, vol. 57, no. 3, pp. 295–303.
- [31] **B. Aiazzi, L. Alparone, S. Baronti, et al.**, 2006, MTF-tailored Multiscale Fusion of High-resolution MS and Pan Imagery, *Photogrammetric Engineering & Remote Sensing*, vol. 72, no. 5, pp. 591–596.
- [32] **J. Lee and C. Lee**, 2010, Fast and Efficient Panchromatic Sharpening, *IEEE Transactions on Geoscience and Remote Sensing*, vol. 48, no. 1, pp. 155–163.
- [33] **C. Ballester, V. Caselles, L. Igual, et al.**, 2006, A Variational Model for P+XS Image Fusion, *International Journal of Computer Vision*, vol. 69, no. 1, pp. 43–58.
- [34] **G. Vivone, L. Alparone, J. Chanussot, et al.**, 2015, A Critical Comparison Among Pansharpening Algorithms, *IEEE Transactions on Geoscience and Remote Sensing*, vol. 53, no. 5, pp. 2565–2586.
- [35] **F. Palsson, J. R. Sveinsson, and M. O. Ulfarsson**, 2014, A New Pansharpening Algorithm Based on Total Variation, *IEEE Geoscience and Remote Sensing Letters*, vol. 11, pp. 318–322.
- [36] **L. Zhang, H. Shen, W. Gong, and H. Zhang**, 2012, Adjustable Model-Based Fusion Method for Multispectral and Panchromatic Images, *IEEE Transactions on Systems, Man, and Cybernetics, Part B (Cybernetics)*, vol. 42, no. 6, pp. 1693–1704.
- [37] **T. Wang, F. Fang, F. Li, and G. Zhang**, 2019, High-Quality Bayesian Pansharpening, *IEEE Transactions on Image Processing*, vol. 28, no. 1, pp. 227–239.

- [38] **S. Boyd, Neal Parikh, Eric Chu, et al.**, 2010, Distributed Optimization and Statistical Learning via the Alternating Direction Method of Multipliers, *Foundations and Trends® in Machine Learning*, vol. 3, no. 1, pp. 1–122.
- [39] **M. Elad, M. A. T. Figueiredo, and Yi Ma**, 2010, On the Role of Sparse and Redundant Representations in Image Processing, *Proceedings of the IEEE*, vol. 98, no. 6, pp. 972–982.
- [40] **A. K. Tanc and E. M. Eksioğlu**, 2016, MRI reconstruction with analysis sparse regularization under impulsive noise, in *2016 24th European Signal Processing Conference (EUSIPCO)*, pp. 538–541.
- [41] **J. Mairal, M. Elad, and G. Sapiro**, 2008, Sparse Representation for Color Image Restoration, *IEEE Transactions on Image Processing*, vol. 17, no. 1, pp. 53–69.
- [42] **M. Elad and M. Aharon**, 2006, Image Denoising Via Sparse and Redundant Representations Over Learned Dictionaries, *IEEE Transactions on Image Processing*, vol. 15, no. 12, pp. 3736–3745.
- [43] **Ö. Bayır and E. M. Ekşioğlu**, 2016, Analysis sparsity based single image superresolution, in *2016 24th Signal Processing and Communication Application Conference (SIU)*, pp. 977–980.
- [44] **E. J. Candès, J. K. Romberg, and T. Tao**, 2006, Stable signal recovery from incomplete and inaccurate measurements, *Communications on Pure and Applied Mathematics*, vol. 59, no. 8, pp. 1207–1223.
- [45] **K. Dabov, A. Foi, V. Katkovnik, and K. Egiazarian**, 2007, Image Denoising by Sparse 3-D Transform-Domain Collaborative Filtering, *IEEE Transactions on Image Processing*, vol. 16, no. 8, pp. 2080–2095.
- [46] **A. Danielyan, V. Katkovnik, and K. Egiazarian**, Image Deblurring By Augmented Lagrangian With BM3D Frame Prior, p. 6.
- [47] **A. Danielyan, A. Foi, V. Katkovnik, and K. Egiazarian**, Image And Video Super-Resolution Via Spatially Adaptive Block-Matching Filtering, p. 8.
- [48] **E. M. Eksioğlu**, 2016, Decoupled Algorithm for MRI Reconstruction Using Nonlocal Block Matching Model: BM3D-MRI, *J Math Imaging Vis*, vol. 56, no. 3, pp. 430–440.
- [49] **A. Danielyan, V. Katkovnik, and K. Egiazarian**, 2012, BM3D Frames and Variational Image Deblurring, *IEEE Transactions on Image Processing*, vol. 21, no. 4, pp. 1715–1728.
- [50] **J. M. Bioucas-Dias, A. Plaza, N. Dobigeon, et al.**, 2012, Hyperspectral Unmixing Overview: Geometrical, Statistical, and Sparse Regression-Based Approaches, *IEEE Journal of Selected Topics in Applied Earth Observations and Remote Sensing*, vol. 5, no. 2, pp. 354–379.
- [51] **J. M. P. Nascimento and J. M. B. Dias**, 2005, Vertex component analysis: a fast algorithm to unmix hyperspectral data, *IEEE Transactions on Geoscience and Remote Sensing*, vol. 43, no. 4, pp. 898–910.

- [52] **M. V. Afonso, J. M. Bioucas-Dias, and M. A. T. Figueiredo**, 2011, An Augmented Lagrangian Approach to the Constrained Optimization Formulation of Imaging Inverse Problems, *IEEE Transactions on Image Processing*, vol. 20, no. 3, pp. 681–695.
- [53] **A. Teodoro, J. Bioucas-Dias, and M. Figueiredo**, 2017, Sharpening Hyperspectral Images Using Plug-and-Play Priors, in *Latent Variable Analysis and Signal Separation*, pp. 392–402.
- [54] **S. V. Venkatakrishnan, C. A. Bouman, and B. Wohlberg**, 2013, Plug-and-Play priors for model based reconstruction, in *2013 IEEE Global Conference on Signal and Information Processing*, pp. 945–948.
- [55] **S. H. Chan, X. Wang, and O. A. Elgandy**, 2016, Plug-and-Play ADMM for Image Restoration: Fixed Point Convergence and Applications, *arXiv:1605.01710 [cs]*.
- [56] **L. Wald, T. Ranchin, and M. Mangolini**, 1997, Fusion of satellite images of different spatial resolutions: Assessing the quality of resulting images, *Photogrammetric engineering and remote sensing*, vol. 63, no. 6, pp. 691–699.
- [57] **J. Zhou, D. L. Civco, and J. A. Silander**, 1998, A wavelet transform method to merge Landsat TM and SPOT panchromatic data, *International Journal of Remote Sensing*, vol. 19, no. 4, pp. 743–757.
- [58] **L. Alparone, B. Aiazzi, S. Baronti, et al.**, Multispectral and Panchromatic Data Fusion Assessment Without Reference, 2008. [Online]. Available: <https://www.ingentaconnect.com/content/asprs/pers/2008/00000074/00000002/art00003>. [Accessed: 08-Mar-2019].
- [59] **W. Shi, C. Zhu, Y. Tian, and J. Nichol**, 2005, Wavelet-based image fusion and quality assessment, *International Journal of Applied Earth Observation and Geoinformation*, vol. 6, no. 3, pp. 241–251.
- [60] **L. Wald**, 2000, Quality of high resolution synthesised images: Is there a simple criterion?, in *Third conference "Fusion of Earth data: merging point measurements, raster maps and remotely sensed images"*, Sophia Antipolis, France, pp. 99–103.
- [61] **Z. Wang and A. C. Bovik**, 2002, A universal image quality index, *IEEE Signal Processing Letters*, vol. 9, no. 3, pp. 81–84.
- [62] **E. Eksioğlu and A. Tanc**, 2018, Denoising AMP for MRI Reconstruction: BM3D-AMP-MRI, *SIAM J. Imaging Sci.*, vol. 11, no. 3, pp. 2090–2109.



CURRICULUM VITAE



Name Surname: Ronglei Ji

Place and Date of Birth: HeNan, China, 19.11.1990

E-Mail: jerry52131@gmail.com

EDUCATION:

B.Sc.: 2012, South Central University for Nationalities, China, Optical Information Science and Technology